Clays and Clay Minerals, Vol. 59, No. 4, 378–399, 2011.

REFLECTANCE SPECTROSCOPY OF BEIDELLITES AND THEIR IMPORTANCE FOR MARS

JANICE L. BISHOP[1], WILL P. GATES[2], HEATHER D. MAKAREWICZ[1,3], NANCY K. MCKEOWN[1,4], AND TAKAHIRO HIROI[5]

[1] SETI Institute, 189 Bernardo Avenue, Mountain View, CA 94043, USA
[2] Monash University, Clayton, VIC 3800 Australia
[3] University of Kansas, Lawrence, KS 66045, USA
[4] University of California at Santa Cruz, Santa Cruz, CA 95064, USA
[5] Brown University, Providence, RI 02912, USA

Abstract—Beidellites may exist on Mars and represent intermediate alteration products; their presence would indicate different alteration environments than previously identified because montmorillonite is a low-grade alteration mineral whereas beidellite is a higher-temperature alteration mineral, and often represents a step toward illite formation. The reflectance spectra of beidellites are under study to support their orbital detection on Mars, where spectral signatures of other Al-rich phyllosilicates have been observed. Reflectance spectra of ten Al-rich smectites are presented here which include pure beidellites and Al smectites having compositions between those of beidellite and montmorillonite, and emphasis is placed here on the OH combination bands near 4545 cm^{-1} (2.2 μm) as these vibrational features are commonly used in the identification of phyllosilicates on Mars. Shifts were observed in the Al_2OH band centers, which occur near 4590 cm^{-1} (2.18 μm) in reflectance spectra of beidellite and near 4525 cm^{-1} (2.21 μm) in reflectance spectra of montmorillonite. These are compared with the Al_2OH bending vibrations observed near 941–948 cm^{-1} (10.5–10.6 μm) for beidellite and near 918–926 cm^{-1} (10.8–10.9 μm) for montmorillonite. Although the octahedral site cation composition provides the greatest influence on the vibrational energies of the M_2OH groups, the tetrahedral site cation composition also influences these vibrations. Shifts were observed in the Si–O–Al bending vibrations from 552 and 480 cm^{-1} (18.1 and 20.8 μm) in beidellite spectra to 544 and 475 cm^{-1} (18.4 and 21.0 μm) in montmorillonite spectra. Gaussian modeling of the 4545 cm^{-1} (2.2 μm) bands led to the discrimination of four overlapping bands in each of the ten Al smectite spectra examined in this study. Shifts in the band center and area of the primary spectral band are coordinated with substitution of Al for Si in the tetrahedral sheet. This is consistent with beidellites having a greater tetrahedral layer charge than montmorillonites. The observed spectral differences were sufficiently large that these Al-rich smectites can be differentiated in orbital data of Mars. A pure beidellite-type spectrum is observed in an isolated Al phyllosilicate-bearing outcrop in Libya Montes, a region where Fe-rich smectite is common but Al-rich smectite is rare. Beidellite-type reflectance spectra were also observed in one area of the Nili Fossae region. In contrast, a variety of Al phyllosilicates were found in the ancient rocks at Mawrth Vallis, including some smaller clay-bearing regions exhibiting spectral signatures more consistent with beidellite-like than montmorillonite-like chemistry.

Key Words—Al smectite, Beidellite, CRISM, Mars, Montmorillonite, Orbiter, Nili Fossae.

INTRODUCTION

The spectral properties of beidellites are investigated in order to gain a better understanding of how the structure and chemistry of these Al smectites affects their spectral properties. Visible/near-infrared (VNIR) reflectance spectra of beidellites exhibit an OH combination band due to stretching and bending vibrations of OH connected to the octahedral cations. This band is centered near 4590 cm^{-1} (2.18 μm), which is measurably different from the 4525 cm^{-1} (2.21 μm) band observed in reflectance spectra of montmorillonite (*e.g.* Post and Noble 1993; Bishop *et al.*, 1994; Gates, 2005). Reflectance spectra of smectites with compositions intermediate to beidellite and montmorillonite (biedellite/montmorillonite) exhibit bands centered near 4525 cm^{-1} (2.21 μm) with a shoulder near 4590 cm^{-1} (2.18 μm) (*e.g.* Post and Borer, 2002; Gates, 2005). This asymmetric band observed for intermediate beidellite/montmorillonite reflectance spectra is different from the character of the broader Si-OH band observed in this wavelength region that is often present in opal reflectance spectra as a shoulder-like feature at longer wavelengths, but somewhat more related to that of montmorillonite-kaolinite mixtures (McKeown *et al.*, 2011).

Phyllosilicate-bearing outcrops on Mars exhibit a range of mineralogical and spectral properties (*e.g.*

* E-mail address of corresponding author:
jbishop@seti.org
DOI: 10.1346/CCMN.2011.0590403

Poulet *et al.*, 2005; Bishop *et al.*, 2008b; Mustard *et al.*, 2008; Ehlmann *et al.*, 2009). Many reflectance spectra of these Martian clay-bearing regions exhibit a band near 4545 cm^{-1} (2.2 μm) that is characteristic of Al phyllosilicates, opal, and hydrated silica glass (*e.g.* Milliken *et al.*, 2008b; Noe Dobrea *et al.*, 2010). Another purpose of this study was to provide spectral analyses of beidellites that will facilitate identification of this mineral on the Martian surface in cases when a spectral feature is observed near 4545 cm^{-1} (2.2 μm) and questions arise as to whether it is due to Al phyllosilicates or to hydrated silica.

BACKGROUND

Beidellite was first identified and characterized by Larsen and Wherry (1925) and is named after Beidell, Colorado, where an early sample was collected. Beidellite is differentiated from the other aluminous smectite, montmorillonite, by the degree of tetrahedral and octahedral substitution and resulting distribution of layer charge (*e.g.* Grim, 1968; Schultz, 1969; Brindley and Brown, 1980; Malla and Douglas, 1987; Wilson, 1987; Chamley, 1989; Velde, 1995). These studies employed Li^+ exchange, heat treatment, X-ray diffraction (XRD), and infrared (IR) spectroscopy to differentiate beidellite from montmorillonite. In general, beidellite has greater substitution of Al for Si in the tetrahedral sites and less substitution of ferric or ferrous Fe and Mg for Al in the octahedral sites than does montmorillonite. Thus, beidellites are defined as having greater tetrahedral than octahedral layer charge compared to montmorillonites. Beidellites are structurally similar to nontronites and ferric smectites, having a *trans*-vacant (*M*1 site) dioctahedral array, whereas montmorillonites are usually *cis*-vacant (one of the symmetric *M*2 sites is vacant) (Lanson and Champion, 1991; Lanson and Besson, 1992).

The IR spectral properties of beidellites have been studied and related to those of other phyllosilicates (Farmer, 1974; Grauby *et al.*, 1993; Post and Noble, 1993; Kloprogge *et al.*, 1998; Post and Borer, 2002; Gates, 2005; Kloprogge, 2006). Most of these studies focused on transmission spectra in the mid-IR wavelength range. The focus here is placed instead on reflectance spectra of the OH combination bands in the near-infrared (NIR) wavelength region for comparison with remote sensing data. The NIR reflectance spectra of beidellites have been reported to exhibit bands near 4548–4585 cm^{-1} (2.181–2.199 μm) (Post and Noble, 1993) and near 4577 cm^{-1} (2.185 μm) (Gates, 2005). This band is assigned to Al_2OH combination modes of one stretch and one bend for each Al_2OH site in the structure (*e.g.* Bishop *et al.*, 1994, 2002a, 2002b).

The primary influence on the vibrational energy of the OH bond in smectites is the type of octahedral cation, as summarized in previous studies (*e.g.* Farmer, 1974; Bishop *et al.*, 2002a; Gates, 2005). A secondary influence on the OH bond is the tetrahedral cation composition and the resulting influence on H-bonding. A reduction in charge on the apical O occurs for increased octahedral Al abundance that allows for increased H-bonding to the OH proton (Gates, 2005). An earlier study of OH-stretching bands in micas postulated that the bond strength at the apical O connecting the tetrahedral and octahedral sheets governs the vibrational frequency of the OH bond (Robert and Kodama, 1988). The OH proton was shown (Besson and Drits, 1997a) to form weak H bonds with apical oxygen ions residing across the octahedral vacancy, and those authors postulated that the strength of the H bond is influenced by the presence of isomorphic substitution in octahedral or tetrahedral sites adjacent to the vacant site. Tetrahedral substitution of Al for Si was shown to increase *M*-OH stretching (Besson and Drits (1997b) and bending (Gates, 2005) frequencies, whereas octahedral substitution of Mg for Al tended to decrease the frequencies of these stretching and bending vibrations. From a thermal and XRD study of 83 aluminous smectites, Schultz (1969) suggested that beidellites form due to protonation of the apical oxygens with the H^+ of these OH groups directed toward the vacant octahedral cation sites. Madejová *et al.* (1996) observed a shift in the mid-IR OH-bending vibrations toward higher frequencies (shorter wavelengths) with increasing charge reduction in Al-rich smectites (*e.g.* AlMg-OH to Al_2-OH), interpreting this as introducing more beidellitic character to the spectra, as an increasing proportion of the residual charge resides in the tetrahedral sheet. Gates *et al.* (2000) evaluated reduced-charge smectites using ^{33}Si NMR and found that shifts in band positions were related to the average electronic density of the tetrahedral Si–O bonds.

Additional bands are also present in smectite spectra from 4000 to 4200 cm^{-1} (2.38–2.50 μm) that appear to be associated with tetrahedral substitution (Bishop *et al.*, 2002a). Gates (2005) hypothesized that these bands are due to coupled vibrations of the OH-stretching with the Al_{oct}-O-Si_{tet} modes. These bands are observed near 4104 cm^{-1} (2.44 μm) for beidellites (Gates, 2005), near 4080 cm^{-1} (2.45 μm) for montmorillonites (Petit *et al.*, 2004; Gates, 2005; Bishop *et al.*, 2008a), near 4155 cm^{-1} (2.41 μm) for nontronite (Gates, 2005; Bishop *et al.*, 2008a), and near 4200 cm^{-1} (2.38 μm) for saponite (Bishop *et al.*, 2008b).

METHODS

Samples

Ten natural beidellite and beidellite/montmorillonite samples were studied from a collection of well characterized smectites (Gates, 2005). The samples were purified *via* sediment fractionation and Ca-saturation of the interlayer exchange sites. The origin and

https://doi.org/10.1346/CCMN.2011.0590403 Published online by Cambridge University Press

Table 1. Beidellite sample information.

Sample ID	Name	Mineral	Details
B34 JB919*	Delamar (Glen Silver Pit)	Beidellite	Ca-sat, <0.2 μm (Idaho, USA)
B35 JB920^{+}	SBId-1	Beidellite	Ca-sat, <0.2 μm (Idaho, USA)
B36 JB921*	SBCa-1	Beidellite	Ca-sat, <0.2 μm (California, USA)
B37 JB922^{+}	3rd Bench	Beidellite	Ca-sat, <0.2 μm (Idaho, USA)
B38 JB923^{+}	Cameron	Beidellite	Ca-sat, <0.2 μm (Arizona, USA)
B39 JB924^{+}	Mt Binjour	Beidellite-Montmorillonite	Ca-sat <0.2 μm (Queensland, Australia
B40 JB925*	Binjour Plateau 4a	Beidellite-Montmorillonite	Ca-sat, <0.1 μm (Queensland, Australia)
B41 JB926*	Binjour Plateau 4a	Beidellite-Montmorillonite	Ca-sat, 0.1−0.2 μm (Queensland, Australia)
B42 JB927*	Binjour Plateau 4a	Beidellite-Montmorillonite	Ca−sat, 0.2−0.5 μm (Queensland, Australia)
B43 JB928^{+}	Binjour Plateau 4a	Beidellite-Montmorillonite	Ca−sat, 0.5−2 μm (Queensland, Australia)
JB174"	JP	Montmorillonite	<2 μm (Jelšový Potok, Slovakia)
JB874′	46-E5888	Opal-CT	Natural sample (Virgin Valley, Nevada)

* sample from Gates (2005)
$^{+}$ data prepared for the present study
" sample from Madejová *et al.* (1994) and Bishop *et al.* (2002a)
′ sample collected by S. Hillier, described in McKeown *et al.* (2011)

mineral classification for each sample are presented in Table 1. Beidellites were identified as such using a combination of IR (Post and Borer, 2002) and XRD on the <0.1 μm size fraction by sedimentation as discussed by Gates *et al.* (2002). Many samples were Li-saturated prior to dialysis and washing to ensure their purity. The montmorillonite sample (JB174) used for comparison with these is the <2 μm fraction of a Slovakian montmorillonite from Jelšový Potok (Madejová *et al.*, 1994; Bishop *et al.*, 2002a). The opal-CT sample is from Virgin Valley, Nevada, USA and was prepared by Steve Hillier for a separate study (McKeown *et al.*, 2011).

X-ray diffraction

The XRD patterns were measured on randomly oriented powders back pressed into aluminum sample supports using a Phillips 1710 diffractometer modified with an electronic stepper motor and CuKα radiation source. All samples in this study showed XRD patterns consistent with smectite, with only minor impurities (*e.g.* illite in B35 and B38; apatite in B43; example patterns for three samples are presented in Figure 1).

Chemical analysis

Elemental analyses were performed on most samples (reported as oxides in Table 2) using X-ray fluorescence (XRF) spectrometry on ~1 g of Ca-saturated samples melted in alkali flux after heating to ~1100ºC, as in previous studies (*e.g.* Norrish and Hutton, 1967) and following standard procedures (*e.g.* Battaglia *et al.*, 2006). Chemical analysis of two samples, B35 (JB920) and B38 (JB923), revealed sufficient K_2O to consider the presence of illite, probably as interstratified illite-smectite (I-S). Estimates indicate that ~17% and ~44% of this phase occur in samples B35 and B38, respectively. These levels of impurities may present some error in the chemical relations, but could also potentially provide support for geological implications of beidellite as an intermediary to illitization reactions discussed later.

Insufficient material was available for XRF analysis of one sample (B39/JB924), thus its chemistry was determined from scanning electron microscopy (SEM) and energy dispersive X-ray (EDX) analysis using a Philips XL20 scanning electron microscope operating at 20 kV with a tungsten filament and EDAX Genesis components. Three EDX spectra were collected on

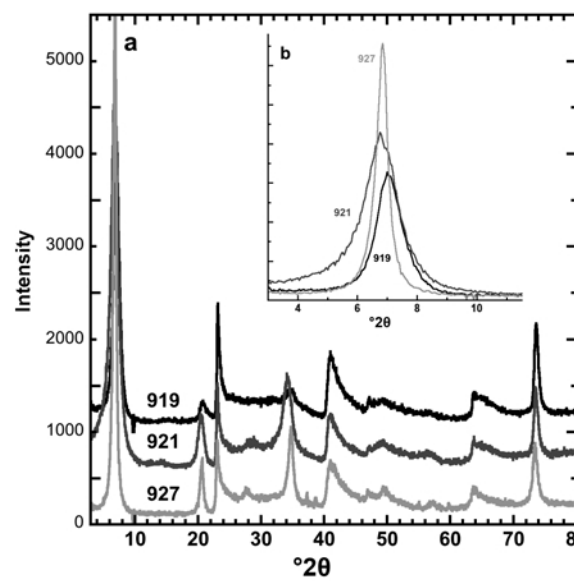

Figure 1. XRD powder patterns for beidellite samples JB919 (B34) and JB921 (B36) and beidellite/montmorillonite sample JB927 (B42): (a) from 3 to 80º2θ and (b) from 3 to 12º2θ.

https://doi.org/10.1346/CCMN.2011.0590403 Published online by Cambridge University Press

Table 2. Major oxide content of ignited (1100ºC) Ca-saturated samples.

Sample	SiO_2	TiO_2	Al_2O_3	Fe_2O_3	MnO	MgO	CaO	Na_2O	K_2O	Sum
B34 JB919*	62.11	0.00	32.09	0.50	0.011	1.330	3.298	0.009	0.711	100.1
B35 JB920^{+}	60.29	0.51	30.96	3.12	0.000	0.932	2.809	0.148	1.228	100.0
B36 JB921*	60.77	0.00	31.99	2.02	0.005	0.859	3.012	0.015	0.660	99.33
B37 JB922^{+}	62.48	0.18	31.60	0.59	0.015	1.209	3.376	0.010	0.607	100.07
B37 JB922^{++}	64.7	0.3	28.7	1.1	n.d.	1.3	3.1	0.0	0.7	99.9
B38 JB923^{+}	57.90	0.21	25.23	8.32	0.020	2.330	2.918	0.009	3.058	99.99
B39 JB924^{+}	66.0	0.3	24.0	2.3	0.0	3.2	4.0	0.0	0.2	100.0
B39 JB924^{+c}	63.7	0.2	26.4	1.2	0.0	3.0	4.4	0.0	0.2	99.1
B40 JB925*	62.93	0.06	24.59	3.30	0.008	2.842	2.832	0.071	0.047	98.81
B41 JB926*	63.77	0.01	26.25	1.71	0.010	3.868	4.052	0.074	0.016	99.76
B42 JB927*	62.62	0.15	25.25	2.44	0.063	4.222	4.749	0.019	0.037	99.54
B43 JB928^{+}	61.57	0.68	22.77	5.42	0.000	4.339	4.558	0.028	0.306	100.0
JB174"	64.52	0.40	23.36	4.20	n.d.	3.55	3.38	0.09	0.35	99.85

The maximum error is expected to be 10% of each elemental analysis; all Fe is shown as Fe_2O_3 and could include both oxidation states of Fe; * as published in Gates (2005); $^{+}$ data prepared for the present study; $^{++}$ chemistry by EDX for the present study; $^{+c}$ XRF equivalent values determined by correcting the EDX values by the difference factor from sample JB922; " chemistry from Madejová *et al.* (1994).

particles (spot sizes between 10 and 50 nm in diameter) positioned within the field of view to maximize the O 1s signal. Counts for each element were converted to oxides and the major oxides were normalized to sum to 100% after ignoring the small residual O 1s signal. The short wavelength of the O 1s X-rays makes direct quantitative analysis of O content challenging. An example SEM image and the corresponding EDX spectra from one location illustrate this procedure (Figure 2). The EDX spectra of the beidellite from the 3rd bench (JB922) were also collected to ensure direct comparison between the two methods. The EDX data gave slightly larger Si, Fe, and Mg abundances and slightly lower Al and Ca abundances. This arises from the need to normalize the EDX values to the O signal, which can be affected by water loss during analysis. The XRF and EDX values from the 3rd bench sample (JB922) were used here to apply a correction factor to the JB924 sample to obtain 'XRF equivalent' values for comparison with the other samples analyzed by XRF. Both sets of data are reported in Tables 2 and 3. Structural formulae calculations (after Bodine, 1987) were based on the chemical analyses assuming full occupancy of the tetrahedral sheet and a 22 oxygen anionic lattice per unit cell (Table 3).

Reflectance spectra

Reflectance spectra were measured on undiluted powders in a horizontal sample dish using a bi-directional VNIR spectrometer and a Nicolet FTIR spectrometer at the Reflectance Experiment LABoratory (RELAB) at Brown University (Providence, Rhode Island, USA) as in past studies (*e.g.* Bishop *et al.*, 2002a). Spectra were measured relative to Halon from 0.3 to 2.6 μm under ambient conditions with 5 nm spectral sampling. Infrared reflectance spectra were measured relative to a textured gold surface in a biconical configuration with 2 cm^{-1} spectral sampling from 1–100 μm in an environment purged of H_2O and CO_2 for 10–12 h. Composite,

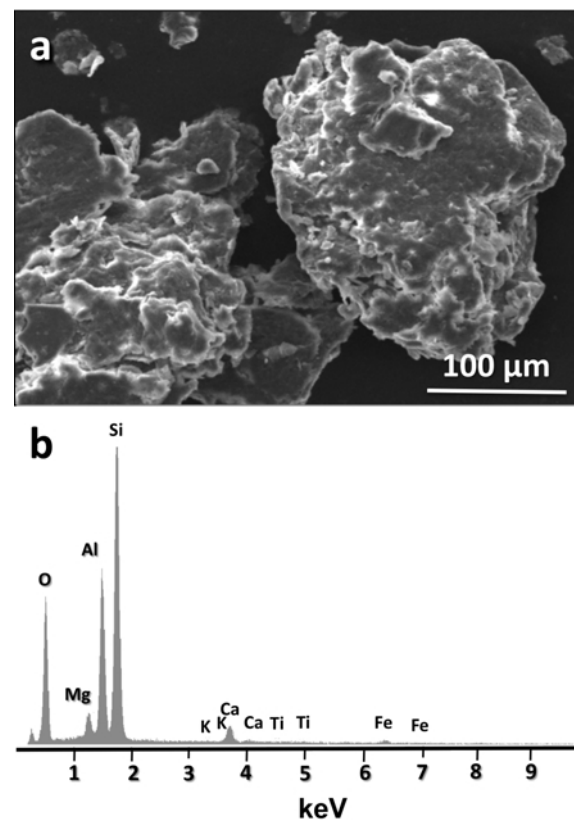

Figure 2. SEM image of the <2 μm fraction of the Mt Binjour smectite (JB924): (a) a high-resolution image showing surface detail of a smectite particle; and (b) an EDX spectrum (one of five) collected from the center of the particle on the right.

https://doi.org/10.1346/CCMN.2011.0590403 Published online by Cambridge University Press

Table 3. Structural formula per $O_{20}(OH)_4$.

Sample ID	Atoms per $O_{20}(OH)_4$					Layer charge characteristics			
	Tetrahedral sites		Octahedral sites			e^- per $O_{20}(OH)_4$			
	Si	Al	Al	Fe	Mg	Tet	Oct	Tot	Tet/oct
B34 JB919 Delamar*	7.29	0.71	3.73	0.05	0.23	0.71	0.23	0.94	3.1
B35 JB920 SBId-1	7.20	0.80	3.56	0.28	0.17	0.80	0.14	0.94	5.7
B36 JB921 SBCa-1*	7.21	0.79	3.69	0.18	0.15	0.79	0.08	0.87	9.9
B37 JB922 3rd bench+	7.35	0.65	3.74	0.05	0.21	0.65	0.21	0.86	3.1
B37 JB922 3rd bench++	7.61	0.39	3.59	0.10	0.23	0.39	0.49	0.88	0.80
B38 JB923 Cameron+	7.14	0.86	2.81	0.77	0.43	0.86	0.40	1.26	2.2
B39 JB924 Mt Binjour+^	7.80	0.20	3.14	0.20	0.57	0.20	0.83	1.03	0.24
B39 JB924 Mt Binjour+c	7.59	0.41	3.29	0.11	0.53	0.41	0.74	1.15	0.55
B40 JB925 BP <0.1*	7.52	0.48	2.99	0.30	0.76	0.47	0.63	1.10	0.75
B41 JB926 BP 0.1–0.2*	7.51	0.46	3.21	0.15	0.68	0.46	0.59	1.05	0.78
B42 JB927 BP 0.2–0.5*	7.48	0.52	3.04	0.22	0.75	0.52	0.71	1.23	0.73
B43 JB928 BP 0.5–2.0+	7.48	0.52	2.74	0.50	0.79	0.52	0.72	1.24	0.72
JB174 JP <2 μm"	7.70	0.30	2.99	0.38	0.63	0.30	0.64	0.94	0.47

The maximum error is expected to be 2% for Si and 5% for the others; * as published in Gates (2005); + data prepared for the present study; ++ from EDX values; +c from XRF equivalent values determined by correcting the EDX values by the difference factor from sample JB922; " determined from values in Madejová *et al.* (1994); tet refers to tetrahedral, oct refers to octahedral, and tot refers to total.

absolute reflectance spectra were prepared by scaling and splicing the FTIR data to the bidirectional data near 1.2 μm.

Spectra were measured of two textures of each sample: fluffy, loose particles (A) and pressed particles (B). The two textures were intended to provide different sample configurations that may be observed on the surface of Mars: loose texture relating to surface dust/soil and compressed texture relating to lithified/consolidated sediments and clay-bearing rocks. Each powder sample was placed in a black teflon dish for spectral measurement. The fluffy samples were prepared by pouring loose powder into the dish, tapping the dish gently to settle the particles, and refilling the dish until full. The surface was not scraped with a spatula. For the pressed samples, a heaping amount of material (about double the volume of the fluffy texture samples) was poured into the Teflon dishes and then compressed until most of the sample fit in the dish using a manual press with a textured glass contact surface. The sample surface was shaved off with a spatula, and then cleaned with a brush.

Gaussian modeling of spectra

Modified Gaussian Modeling (MGM) was performed using new automated procedures (Makarewicz *et al.*, 2009; Parente *et al.*, 2011) based on the MGM technique developed for modeling reflectance spectra of mafic minerals (Sunshine *et al.*, 1990; Sunshine and Pieters, 1993). The Sunshine procedure models both the continuum slope and the absorption bands of interest. Another technique implemented has been a double linear continuum removal (Hiroi and Pieters, 1998). In the present study the continuum was modeled with a convex hull as described by Parente *et al.* (2011). Quantitative analyses were performed using MGM analyses of pyroxene mineral mixtures (Sunshine and Pieters, 1993) and pyroxene and plagioclase in Lunar soils (Noble *et al.*, 2006).

This method has been extended to model spectral features due to phyllosilicates using Gaussians from 0.5 to 2.6 μm (Makarewicz *et al.*, 2009; Parente *et al.*, 2011). An automatic parameter initialization step, based on the features of the spectrum being modeled, was used

https://doi.org/10.1346/CCMN.2011.0590403 Published online by Cambridge University Press

in order to determine the optimum number of Gaussians needed to fit the spectral features. This was accomplished by computing the 1st and 2nd derivatives of the reflectance spectrum and identifying local extrema and inflection points to automatically select starting points for the initial Gaussian parameters. This differs from the Sunshine method that requires initial estimates of the Gaussian parameters from the user. Both methods then iteratively determine the best-fit Gaussians for the spectrum.

CRISM spectra

The Compact Reconnaissance Imaging Spectrometer for Mars (CRISM) instrument on the Mars Reconnaissance Orbiter (MRO) spacecraft acquires reflectance spectra in a high-resolution targeted mode using two detectors: a VNIR detector covering the spectral range 0.36 to 1.05 μm and an IR detector covering 1.00 to 3.92 μm (Murchie *et al.* 2007, 2009). Full-resolution targeted (FRT) images include 544 channels across the full spectral range from 0.36 to 3.92 μm with a spectral sampling of 6.5 nm in ~10–12 km wide swaths at ~18 m/pixel spatial resolution. For this study, CRISM image processing included subtracting the instrument background, dividing by processed measurements of the internal calibration standard, and dividing the at-sensor radiance by the solar radiance. The resulting I/F image was divided by the cosine of the incidence angle to account for photometric effects. In addition, the effects of atmospheric molecular opacity were minimized by dividing each spectrum by a scaled atmospheric spectrum derived from a CRISM image acquired over Olympus Mons. The CRISM I/F spectra were ratioed to spectrally neutral regions in the same column and smoothed as in previous studies (*e.g.* McKeown *et al.*, 2009) in order to better illustrate the spectral features of interest related to surface properties.

RESULTS

Reflectance spectra of loose and compressed textures of beidellites

Reflectance spectra of three beidellites prepared with loose and pressed textures (Figure 3a) show that spectra of the loose samples exhibit greater reflectance values at

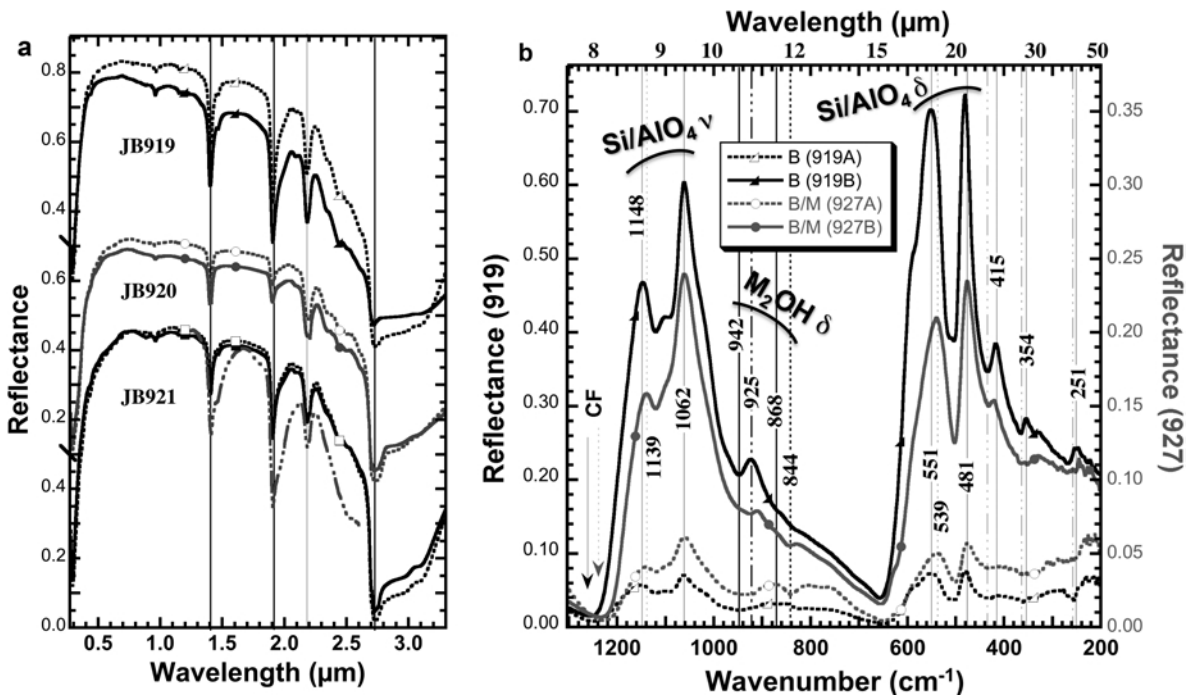

Figure 3. Reflectance spectra of beidellite samples measured with loose ("A", dashed line, open symbols) and pressed ("B", solid line, closed symbols) textures. (a) VNIR spectra of three beidellites from 0.3 to 3.3 μm. Each pair of spectra is similar to the loose spectrum having somewhat brighter reflectance. The pressed texture might better simulate cemented clays or clay-bearing rocks. Each pair of AB texture spectra is offset for clarity. A VNIR spectrum of sample JB921 measured under ambient conditions is shown in a dash dot pattern and exhibits stronger water bands near 1.4 and 1.9 μm due to adsorbed water. (b) Mid-IR spectra of one beidellite and one beidellite/montmorillonite from 200–1300 cm^{-1} (~7.7–50 μm). The compressed spectra exhibit substantially greater reflectance in this region. Small shifts are observed in the Si/AlO_4 stretching and bending modes for the beidellite and beidellite/montmorillonites. A bigger shift is observed in the Al_2OH bending vibration from 942 cm^{-1} for beidellite JB919 to 925 cm^{-1} for beidellite/montmorillonite JB927.

https://doi.org/10.1346/CCMN.2011.0590403 Published online by Cambridge University Press

NIR wavelengths and exhibit greater spectral contrast near 3 μm (~3200-3400 cm^{-1}) than their pressed counterparts. The pressed sample texture may be more consistent with cemented soils or clay-bearing rocks compared to the commonly used loose sample texture for reflectance measurements of particulate samples; however, both sets of spectra in the present study exhibited similar spectral features. The NIR bands due to structural OH occurred near 1.4, 2.2, and 2.7 μm (~7140, 4545, and 3700 cm^{-1}), whereas bands due to interlayer and/or adsorbed water occurred near 1.4, 1.9, and 2.7–3.2 μm (~7140, 5260, and 3700–3125 cm^{-1}) (*e.g.* Hunt and Salisbury, 1970; Bishop *et al.*, 1994). Most spectra presented in this study were measured after purging H_2O from the spectrometer sample chamber overnight, which was shown to remove most of the adsorbed water from the samples (Bishop *et al.*, 1994). One spectrum measured under ambient conditions was analyzed for comparison (Figure 3a). The ambient spectrum of beidellite JB921 exhibited much stronger features near 1.4 and 1.9 μm (~7140 and 5260 cm^{-1}) due to water, whereas the 2.2 μm (~4545 cm^{-1}) band was unchanged, or perhaps reduced in intensity due to masking from the wings of the large and overlapping ~3 μm (~3200–3400 cm^{-1}) water bands. Due to the restricted moisture levels on Mars (Farmer *et al.*, 1977), adsorbed water cannot be abundant. Thus, measuring reflectance spectra of clay minerals in an environment where the adsorbed water is minimized is expected to represent better the CRISM spectra of these minerals on Mars.

Sample texture and bulk density/porosity have a much greater influence on the spectral brightness at mid-IR wavelengths. Mid-IR reflectance spectra of the pressed beidellite samples exhibited significantly stronger features than spectra of the loosely prepared samples (Figure 3b). The band centers for the strong reststrahlen bands occurred near 1148, 1062, 551, and 481 cm^{-1} or 8.7, 9.4, 18.1, and 20.8 μm for beidellite and near 1139, 1062, 539, and 481 cm^{-1} or 8.8, 9.4, 18.6, and 20.8 μm for intermediate beidellite/montmorillonite samples. The Christiansen feature occurred near 1250 cm^{-1} (8.0 μm) for beidellite and near 1230 cm^{-1} (8.1 μm) for beidellite/montmorillonite. The positions of these features were similar for the spectra of samples with both textures. Some of the weaker bands (*e.g.* Al_2OH bending vibrations) occurred as absorptions or reflectance troughs on the wings of the reststrahlen bands. These features exhibited some differences in the spectra of the loose textured material and compressed texture samples. The feature near 250 cm^{-1} (40 μm) appeared as an absorption band in the reflectance spectra of the loose material and as a reflectance peak in the spectra of the compressed material. This difference is due to variation in the single scattering albedo and whether the particles are scattering individually (loose textures) or as a surface (pressed texture), and is consistent with previous spectral studies of the effects of mineral texture (Salisbury *et al.*, 1991). Transmittance spectra of smectites exhibit absorptions for the Si–O and OH bands (*e.g.* Farmer, 1974), whereas reflectance spectra of smectites exhibit reflectance peaks for the Si–O bands and absorptions for the OH bands. Whether reflectance peaks or absorption bands are observed depends on the particle size and refractive index of the material (Salisbury and Wald, 1992).

Near-infrared combination and overtone vibrations

Visible/near infrared reflectance spectra for loose particulate samples of two beidellites and two intermediate beidellite/montmorillonites (Figure 4) were compared to spectra of montmorillonite and opal. The dominant NIR absorptions in Al smectite spectra as summarized by Bishop *et al.* (1994) are due to a bound H_2O stretching overtone near 1.41 μm, an OH stretching overtone near 1.41 μm (7092 cm^{-1}), an H_2O stretch+bend combination near 1.91 μm (5235 cm^{-1}), and an OH stretch+bend combination near 2.18–2.21 μm (4525–4587 cm^{-1}). In addition, the OH stretching

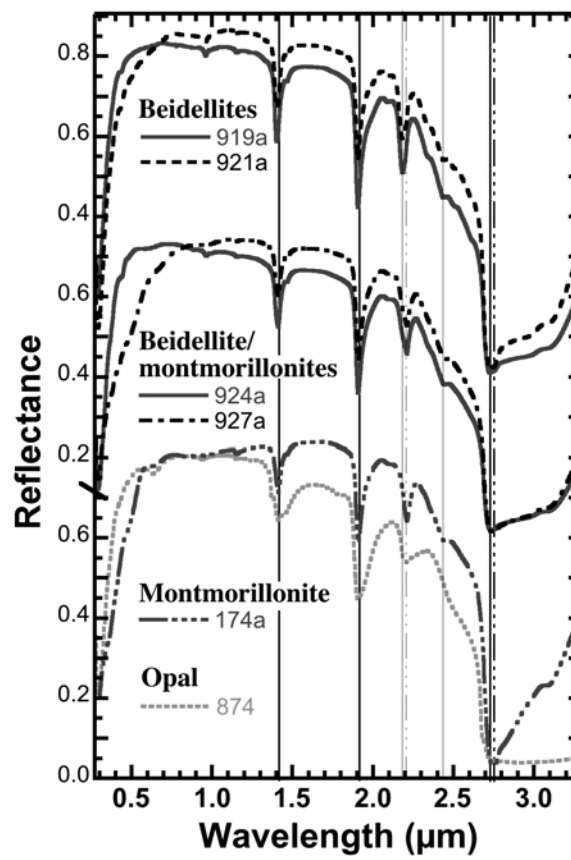

Figure 4. Reflectance spectra of selected beidellites, beidellite/montmorillonites, montmorillonite, and opal from 0.3 to 3.3 μm. All of these spectra exhibit bands near 1.4, 1.9, 2.2, and 2.7–3.2 μm due to OH and H_2O. The spectra are offset for clarity.

https://doi.org/10.1346/CCMN.2011.0590403 Published online by Cambridge University Press

fundamental absorption occurs near 2.7–2.8 μm (3501–3703 cm^{-1}), the H_2O symmetric and asymmetric stretching bands occur near 2.7–3.1 μm (3226–3703 cm^{-1}) for a distribution of water sites, and the H_2O bending overtone near 3.2 μm (3125 cm^{-1}) (Figure 4). Reflectance spectra of opal have generally similar features related to Si-OH and H_2O species (Anderson and Wickersheim, 1964).

Differences were detected in the OH-stretching vibrations for beidellite and montmorillonite (Figure 5). The OH-stretching overtone occurred at 1.399–1.401 μm (7138-7148 cm^{-1}) for the beidellites in the present study, at 1.412–1.413 μm (7077–7082 cm^{-1}) for the intermediate beidellite/montmorillonites, and at 1.413 μm (7082 cm^{-1}) for the JP montmorillonite (Figure 5a, Table 4). The corresponding OH-stretching vibrations exhibited a similar trend in shifting from shorter wavelength (higher frequency) vibrational bands for beidellite spectra to longer wavelength (lower frequency) vibrational bands for montmorillonite spectra (Figure 5b).

The reflectance spectrum of pure beidellite had a band centered near 2.18 μm (4587 cm^{-1}), while smectites exhibiting intermediate beidellite/montmorillonite compositions in the present study exhibited a dominant band near 2.21 μm (4525 cm^{-1}) with an additional band or shoulder near 2.18 μm (4587 cm^{-1}) (Figure 6). Montmorillonite spectra commonly exhibit a band centered near 2.21 μm (4525 cm^{-1}) and often display a shoulder toward longer wavelengths if sufficient Fe or Mg is present in the octahedral sites (*e.g.* Bishop *et al.*, 1993, 2002a; Gates, 2005). Opal spectra also have a band centered near 2.21 μm (4525 cm^{-1}) (Figure 6) that can be highly asymmetric,

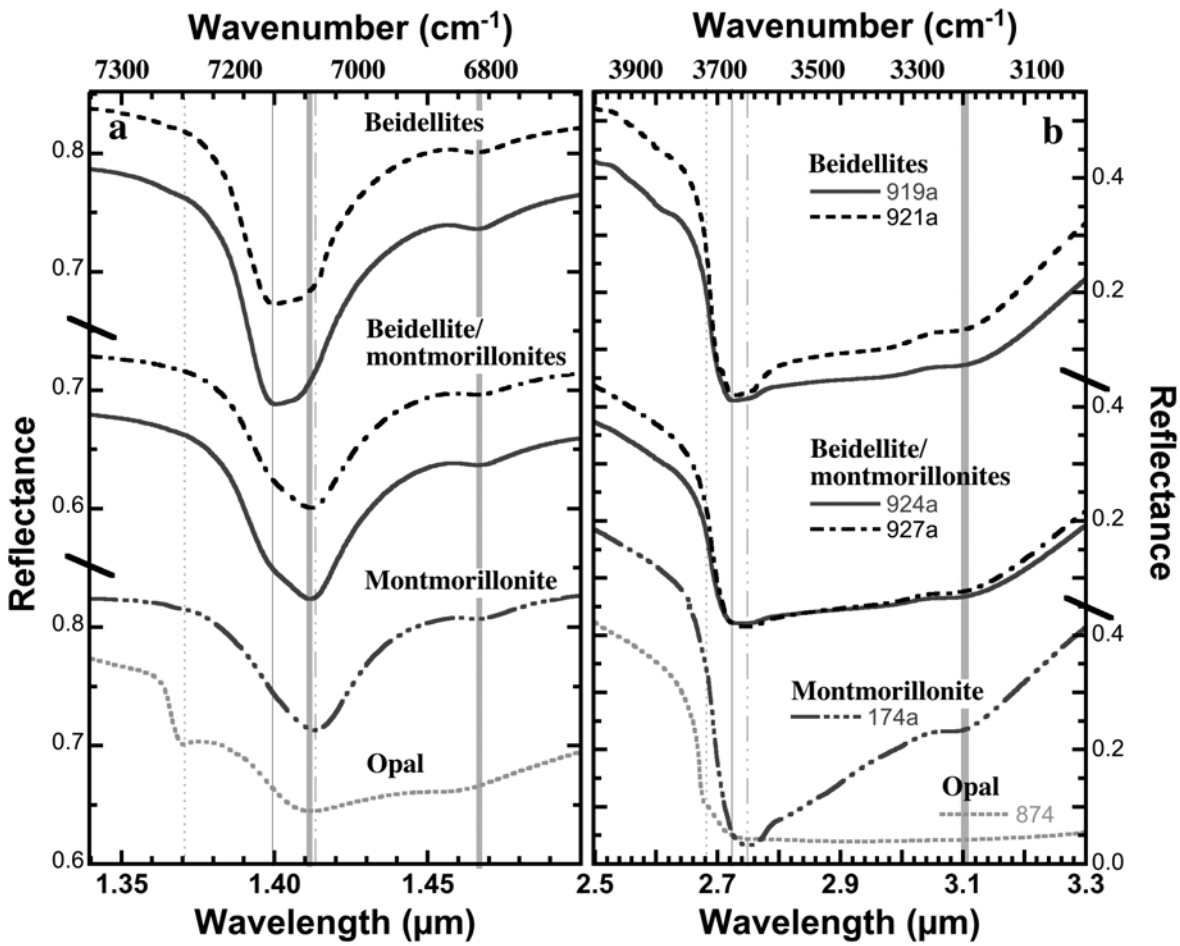

Figure 5. Reflectance spectra of selected beidellites, beidellite/montmorillonites, montmorillonite, and opal highlighting the OH stretching vibrations: (a) the OH-stretching overtone region from 1.34 to 1.50 μm; and (b) the OH stretching region from 2.5 to 3.3 μm. Shifts in the OH-stretching vibrations are observed from near 1.40 and 2.72 μm for beidellite to near 1.41 and 2.75 μm for montmorillonite. The H_2O stretching overtones are marked in light gray for bound (~1.41 μm) and adsorbed (~1.47 μm) H_2O in smectites in part a and the H_2O bending overtone is marked in light gray near 3.1 μm in part b. The H_2O stretching vibrations were broadly distributed from ~2.7 to 3 μm (not marked).

https://doi.org/10.1346/CCMN.2011.0590403 Published online by Cambridge University Press

Table 4. Band centers from Gaussian modeling and related features.

Sample ID	OH combination bands				Measured OH δ (cm^{-1})		Calculated OH ν (cm^{-1})
	Band #	OH ν+δ (μm)	OH ν+δ FWHM	OH ν+δ (cm^{-1})			
B34 JB919A	1	2.177	0.0262	4593	946		3647
B34 JB919A	2	2.189	0.0451	4568	918	sh	3650
B34 JB919A	3	2.204	0.0187	4537			
B34 JB919A	4	2.232	0.0202	4480			
B35 JB920A	1	2.169	0.0308	4610	947		3663
B35 JB920A	2	2.196	0.0512	4554	920	sh	3634
B35 JB920A	3	2.208	0.0093	4529			
B35 JB920A	4	2.241	0.0212	4463			
B36 JB921A	1	2.177	0.0294	4594	941		3653
B36 JB921A	2	2.191	0.0498	4564	918	sh	3656
B36 JB921A	3	2.208	0.0098	4530			
B36 JB921A	4	2.233	0.0194	4477			
B37 JB922A	1	2.175	0.0223	4598	942		3656
B37 JB922A	2	2.186	0.0443	4574	918	sh	3656
B37 JB922A	3	2.208	0.0087	4529			
B37 JB922A	4	2.219	0.0316	4507			
B38 JB923A	1	2.181	0.0311	4585	928		3657
B38 JB923A	2	2.211	0.0481	4522	919	sh	3603
B38 JB923A	3	2.208	0.0000	4529			
B38 JB923A	4	2.249	0.0340	4447			
B39 JB924A	1	2.178	0.0301	4592	945	sh	3647
B39 JB924A	2	2.208	0.0433	4530	928		3602
B39 JB924A	3	2.213	0.0150	4519			
B39 JB924A	4	2.243	0.0261	4457			
B40 JB925A	1	2.178	0.0303	4591	945	sh	3646
B40 JB925A	2	2.209	0.0415	4527	924		3603
B40 JB925A	3	2.213	0.0140	4519			
B40 JB925A	4	2.243	0.0263	4458			
B41 JB926A	1	2.177	0.0301	4592	945	sh	3647
B41 JB926A	2	2.207	0.0431	4531	918	sh	3613
B41 JB926A	3	2.213	0.0157	4518			
B41 JB926A	4	2.241	0.0282	4463			
B42 JB927A	1	2.182	0.0324	4583	939	sh	3644
B42 JB927A	2	2.210	0.0339	4525	918	sh	3607
B42 JB927A	3	2.213	0.0135	4519			
B42 JB927A	4	2.239	0.0289	4466			
B43 JB928A	1	2.185	0.0327	4576	940	sh	3636
B43 JB928A	2	2.210	0.0297	4525	923		3602
B43 JB928A	3	2.213	0.0107	4519			
B43 JB928A	4	2.237	0.0296	4469			

$OH_{\nu+\delta}$ = OH-stretching plus bending combination band; OH_{ν} = OH-stretching vibration; OH_{δ} = OH bending vibration; FWHM = full width at half maximum, sh = shoulder feature.

depending on the degree of H-bonding (*e.g.* Anderson and Wickersheim, 1964; Milliken *et al.*, 2008a). Weak bands were also observed in beidellite spectra near 2.34 and 2.44 μm (~4100 and 4275 cm^{-1}) and in montmorillonite spectra near 2.45 μm (~4080 cm^{-1}).

Mid-IR OH-bending vibrations

Mid-IR reflectance spectra (Figure 7) indicated a shift in the Al_2OH bending band from ~920 cm^{-1} (~10.9 μm) for montmorillonite to ~940–942 cm^{-1} (~10.6 μm) for beidellite. Differences were also observed in the band centers for the AlMgOH and AlFeOH vibrations for beidellites and montmorillonites. A band was observed near 868 cm^{-1} (~11.5 μm) in the reflectance spectrum for the beidellite sample JB919a and a shoulder was observed here for the beidellite JB921a spectrum. In contrast, the montmorillonite and beidellite/montmorillonite reflectance spectra exhibited bands near 844 cm^{-1} (~11.8 μm). Although the NIR OH combination band for opal appeared near the Al smectite band, the mid-IR OH-bending vibration occurred near 816 cm^{-1} (~12.2 μm), a much lower frequency.

Mid-IR Si/AlO_4 bending and stretching vibrations

Mid-IR reflectance spectra of silicate minerals are dominated by SiO_4 reststrahlen bands near 500 and

https://doi.org/10.1346/CCMN.2011.0590403 Published online by Cambridge University Press

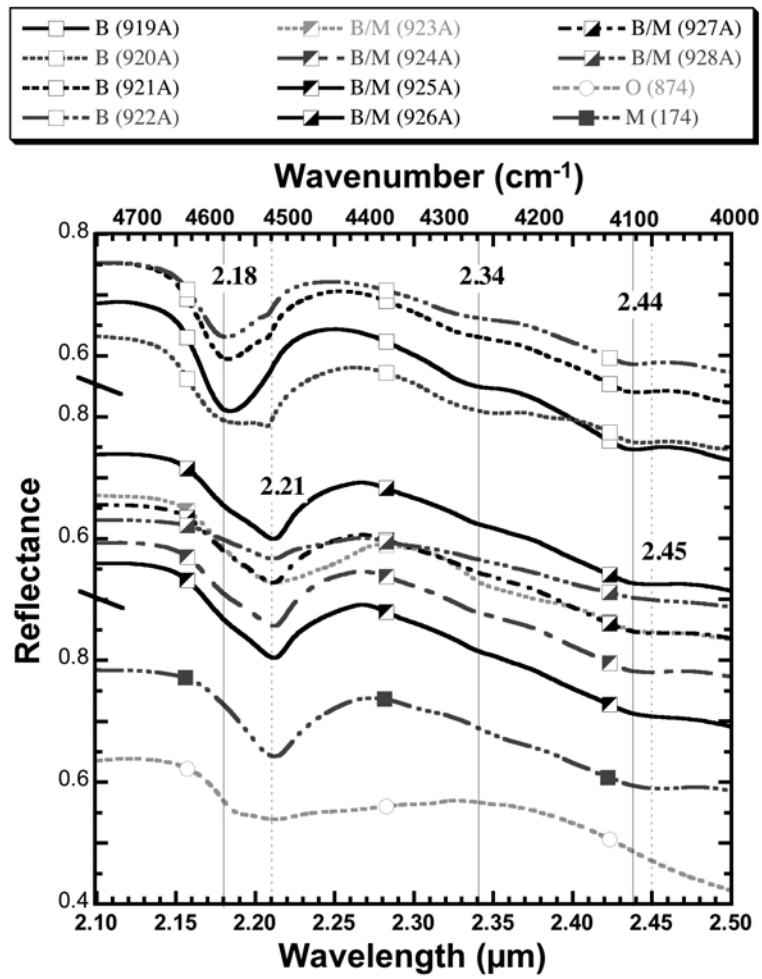

Figure 6. Reflectance spectra of beidellites and beidellite/montmorillonites from 2.1 to 2.5 μm highlighting the region of OH-combination bands. Montmorillonite and opal are also shown for comparison and the spectra are offset for clarity. The beidellite spectra have a band centered at 2.18 μm, while the montmorillonite and opal spectra have a band centered near 2.21 μm.

1100 cm^{-1} (~9.1 and 20 μm) in the surface scattering regime (*e.g.* Salisbury, 1993). The silicate reststrahlen features generally occur as multiple bands for clay minerals (*e.g.* Salisbury, 1993). The SiO_4 bending vibration is observed as a doublet for dioctahedral clay minerals but as a single band for trioctahedral clay minerals (*e.g.* Farmer, 1974; Russell and Fraser, 1994), presumably due to asymmetry in the structure from the octahedral holes. Substitution of Al for Si in some tetrahedral sites results in further loss of symmetry and, therefore, also influences the vibrations due to AlO_4 groups in addition to SiO_4 groups.

This lowering of symmetry gives not only $Al_{oct}–O–Si_{tet}$, but also $Al_{oct}–O–Al_{tet}$ and $M_{oct}–O–Si/Al_{tet}$ bending modes for *M* other than Al. Mid-IR reflectance spectra of beidellites exhibited a doublet at 551 and 481 cm^{-1} (~18.2 and 20.8 μm), whereas montmorillonite spectra contained a doublet closer to 533 and 472 cm^{-1} (~18.8 and 21.2 μm) (Figure 8). The intermediate beidellite/montmorillonite samples gave spectral features at positions between these two sets. In contrast, the spectrum of opal in this region exhibits only one Si–O bending vibration near 480 cm^{-1} (~20.8 μm). Although not the focus of this study, the $M_{oct}–O–Si/Al_{tet}$ vibrational modes where *M* is a trioctahedral cation (*e.g.* Mg) give rise to only a single band, rather than a doublet in this region (*e.g.* Stubican and Roy, 1961; Michalski *et al.*, 2005).

Similar variations were observed in the stretching modes of the SiO_4 and AlO_4 groups (Figure 3b). Beidellite spectra contained a doublet at 1148 and 1062 cm^{-1} (8.71 and 9.42 μm), whereas the intermediate beidellite/montmorillonite spectra had a doublet at 1139 and 1062 cm^{-1} (8.78 and 9.42 μm).

Mid-IR low-energy vibrations

Additional IR absorptions were observed on the flanks of the $(Si_{1-x}Al_x)O_4$ bending vibrations. These included a weak shoulder feature near 590–620 cm^{-1} (~16–17 μm) between the reflectance minimum near

https://doi.org/10.1346/CCMN.2011.0590403 Published online by Cambridge University Press

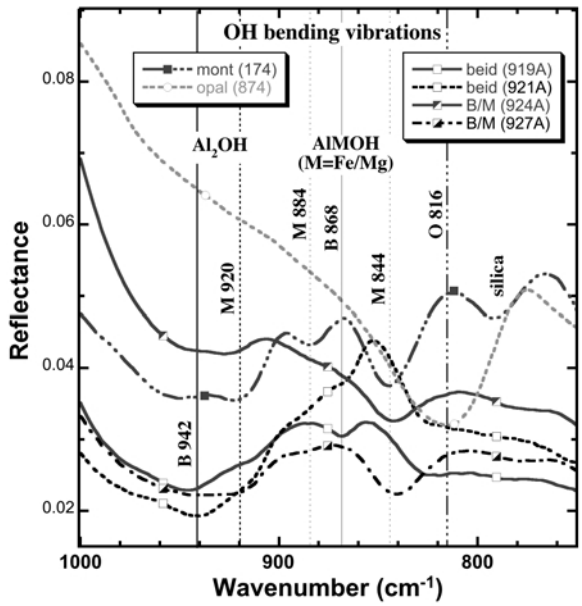

Figure 7. Mid-IR reflectance spectra of selected beidellites, beidellite/montmorillonites, montmorillonite, and opal from 750 to 1000 cm^{-1} highlighting the region of OH-bending vibrations. The beidellite spectra have bands at 942 and 868 cm^{-1} (labeled "B"), while montmorillonite spectra have bands near 920, 884, and 844 cm^{-1} (labeled "M"). Spectra of the beidellite/montmorillonite samples are more similar to the montmorillonite spectrum. Opal has one broad band near 816 cm^{-1} and hydrated silica has a band near 790 cm^{-1} (labeled "O").

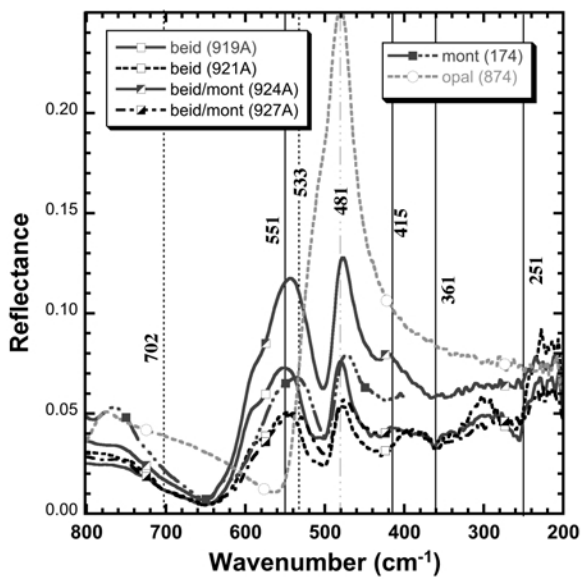

Figure 8. Mid-IR reflectance spectra of selected beidellites, beidellite/montmorillonites, montmorillonite, and opal from 200–800 cm^{-1}. This region shows the Si–O–*M* bending modes near 480 and 550 cm^{-1} and also the out-of-plane Al–O bending mode near 700 cm^{-1}. Beidellite spectra in this region have additional features near 256 and 361 cm^{-1}.

650 cm^{-1} (~15.4 μm) and the reflectance peak near 550 cm^{-1} (~18.2 μm) that is similar to a feature in transmission spectra of montmorillonite and attributed to Mg_{oct}–O–Si_{tet} (Madejová *et al.*, 1996). A shoulder occurred near 600 cm^{-1} (~16.7 μm) in the reflectance spectra of intermediate beidellite/montmorillonite and near 590 cm^{-1} (~16.9 μm) in the reflectance spectra of beidellite (Figures 3b, 8). Additional reflectance peaks were observed near 415, 354, and 251 cm^{-1} (~24.1, 28.2, and 39.8 μm) in the beidellite spectra that are probably due to lattice deformations and are much stronger in the spectra of the compressed samples (Figure 3b). Previous studies have noted an absorption in transmission spectra of beidellites near 420–430 cm^{-1} (23.2–23.8 μm) (Farmer, 1974; Kloprogge, 2006) and near 411–421 cm^{-1} (23.7–24.3 μm) in reflectance spectra (Post and Borer, 2002; Gates, 2005).

Gaussian modeling

Gaussian modeling was performed using an automated method on the overlapping bands near 2.15 to 2.25 μm (~4440–4650 cm^{-1}) in order to characterize better this absorption feature and associate the individual bands with the mineral chemistry. The resulting fit was then analyzed and the number of Gaussians used in the model was varied until the residuals were highly correlated after automated fitting as in previous studies (Makarewicz *et al.*, 2009; Parente *et al.*, 2011). Examples of the Gaussian modeling results are shown for spectra of the beidellite samples JB919A, JB920A, and JB921A (Figure 9) and the intermediate beidellite/montmorillonite samples JB924A, JB925A, and JB927A (Figure 10). Four bands were fit with centers near 2.18, 2.19–2.21, 2.21, and 2.23 μm (~4587, 4525–4570, ~4525, ~4485 cm^{-1}). These bands were determined within the fitting algorithm and were not pre-assigned by the user or constrained in any way. Band 1 was attributed to beidellite, band 2 appeared to span beidellite and montmorillonite, and bands 3–4 were attributed mostly to montmorillonite. Variations in the centers and areas of these four bands were ascribed to differences in the OH-bonding energy resulting from the types of cations occupying the octahedral and tetrahedral sites.

DISCUSSION

The present study investigated relationships between the OH combination bands near 2.2 μm (~4545 cm^{-1}) and the OH-bending vibrations near 10–12 μm (~830–1000 cm^{-1}). Gaussian modeling of the 2.2 μm region enabled more precise examination of the vibrations due to individual Al*M*OH (*M* = Al, Fe, Mg) bonds. Quantification of the variations in the amount of Al in tetrahedral sites and Fe and Mg in octahedral sites (Table 3) for this sample suite enabled characterization of these features.

https://doi.org/10.1346/CCMN.2011.0590403 Published online by Cambridge University Press

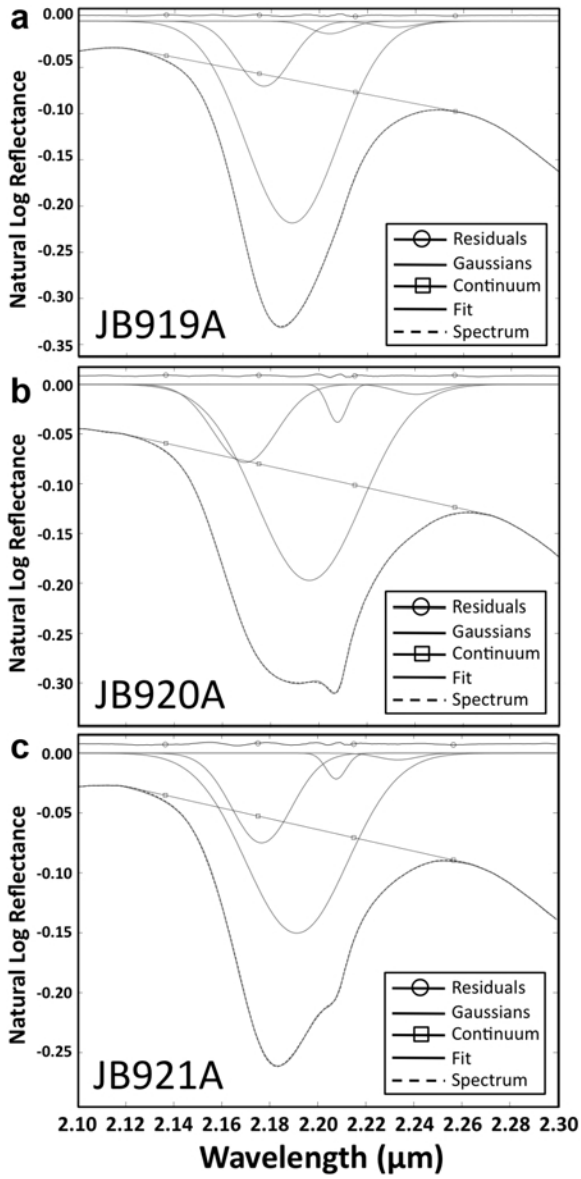

Figure 9. Plots of Gaussian modeling results for three beidellite spectra. Each spectrum is processed with a continuum removal and then fit by four bands. The residual error is given at the top of each plot.

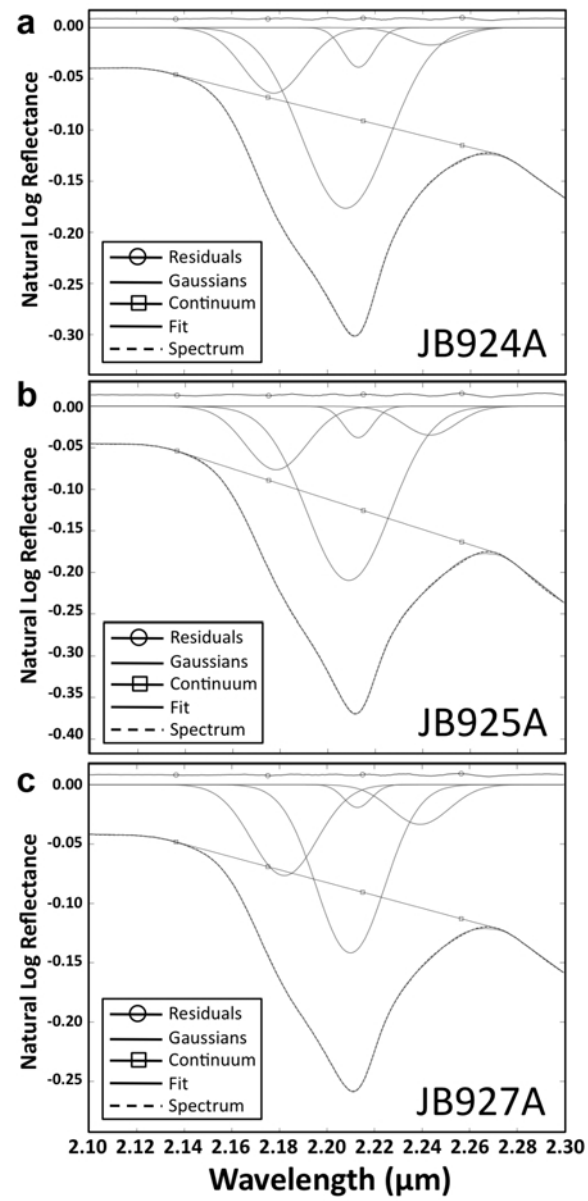

Figure 10. Plots of Gaussian modeling results for three beidellite/montmorillonite spectra. Each spectrum is processed with a continuum removal and then fit by four bands. The residual error is given at the top of each plot.

Correlating spectral features with sample chemistry

The four bands established in the Gaussian modeling of beidellites and intermediate beidellite/montmorillonite samples have been correlated with chemistry for samples with assigned octahedral and tetrahedral cation populations (Gates, 2005). Band centers for the four bands determined in the Gaussian modeling (Table 4) were also compared with the amount of Si in tetrahedral sites for several samples (Figure 11a). The centers for bands 1 (2.169–2.185 μm or 4577–4610 cm^{-1}) and 3 (2.204–2.213 μm or 4519–4537 cm^{-1}) were not found to vary much with Al substitution for Si, while the centers for bands 2 (2.186–2.211 μm or 4523–4575 cm^{-1}) and 4 (2.219–2.249 μm or 4506–4446 cm^{-1}) varied to a greater extent with Al substitution for Si. The minimum band center value occurred for Si abundance of ~7.3 (Al ~0.7) but increased for smaller Si values (greater Al values). Band 2 shifted from 2.191 μm (4564 cm^{-1}) for sample JB921, the SBCa-1 beidellite from California with 7.21 Si and 0.79 Al in the tetrahedral sites per formula unit, to a band center of 2.209 μm (4527 cm^{-1}) for sample JB925, the Binjour 4a beidellite-montmorillonite from Queensland with 7.52 Si and 0.48 Al in the tetrahedral sites per formula unit.

https://doi.org/10.1346/CCMN.2011.0590403 Published online by Cambridge University Press

Band-area ratios were determined as the area of each band divided by the area of all bands. The area ratio was greatest for band 2 at 60–80% of the total area (Figure 11b). Band 1 contributed ~15–30% of the total area and bands 3 and 4 were <10% of the total area (Figure 11b). The band centers and area ratios for the same bands 1–4 from the Gaussian modeling were compared to Al abundance in the octahedral sites in Figure 12. The centers for bands 1, 3, and 4 all shifted toward longer wavelengths with increasing substitution of Fe and Mg for Al (Figure 12a). The center for band 2 also shifted towards longer wavelengths with increasing octahedral substitution for Al but the trend was less consistent (Figure 12a). The area ratios for bands 3 and 4 showed generally consistent trends with octahedral substitution but comprised only a minor amount of the total band area. The area ratios for bands 1 and 2 followed opposite trends at higher and lower octahedral substitution levels (and also higher and lower tetrahedral substitution levels), suggesting that these two bands were compensating for each other (Figures 11b, 12b). In other words, as one band area ratio increased the other decreased. Multiple regression analysis of bands 2 and 3, incorporating the contributions of tetrahedral and octahedral Al content (Figure 13), indicated that not only can the positions of these bands be accurately predicted from beidellite/montmorillonite chemistry, but that the tetrahedral and octahedral aluminum contents can be reasonably predicted from the spectra, providing a potentially useful tool for remote sensing. Future studies will test fixing the centers of bands 1–4 to determine whether it improves the separation of the bands due to OH vibrations in beidellite and montmorillonite.

The Gaussian modeling data showed that the Al-smectites with greater amounts of Fe and Mg in octahedral sites had greater contributions in bands 3 and 4 centered near 2.21 and 2.24 μm (4525 and 4464 cm^{-1}), respectively. These samples with elevated Fe and Mg also had the lowest tetrahedral Al-for-Si substitution and were classified as intermediate beidellite/montmorillonite smectites. Band 2 contributed the bulk of the OH combination feature and correlated best with tetrahedral Al for Si substitution. The center of this band shifted from ~2.19 μm (4566 cm^{-1}) for beidellite samples with low Mg-for-Al substitution in octahedral sites and high Al substitution in tetrahedral sites to a center of ~2.21 μm (4525 cm^{-1}) for intermediate beidellite/montmorillonite samples with greater Fe/Mg-for-Al substitution in octahedral sites and lower Al-for-Si substitution in tetrahedral sites.

Estimating OH vibrational bands from measured and modeled data

Gaussian modeling of the OH stretch + bend combinations resulted in centers and full width at half maximum values for four individual bands (Table 4).

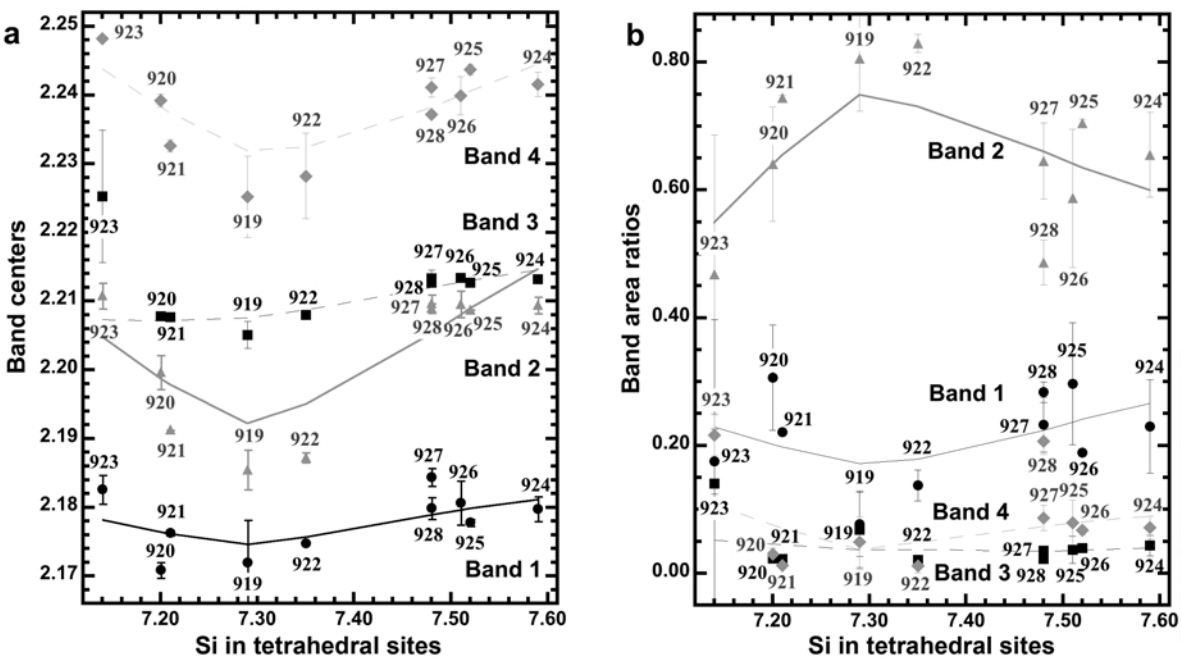

Figure 11. Comparisons of the spectral features with Si abundance in the tetrahedral sites: (a) band center *vs.* Si; and (b) band area ratios *vs.* Si. These data show the greatest shifts in the band center for band two (centered near 2.19–2.21 μm) with varying amounts of substitution for Si in the tetrahedral sites. Band two has the greatest area of all four bands and increases with decreasing Si (increasing Al substitution). Error bars are given from the Gaussian fits. Note that the XRF equivalent value was used for sample JB924 for consistency throughout the chemical analyses.

https://doi.org/10.1346/CCMN.2011.0590403 Published online by Cambridge University Press

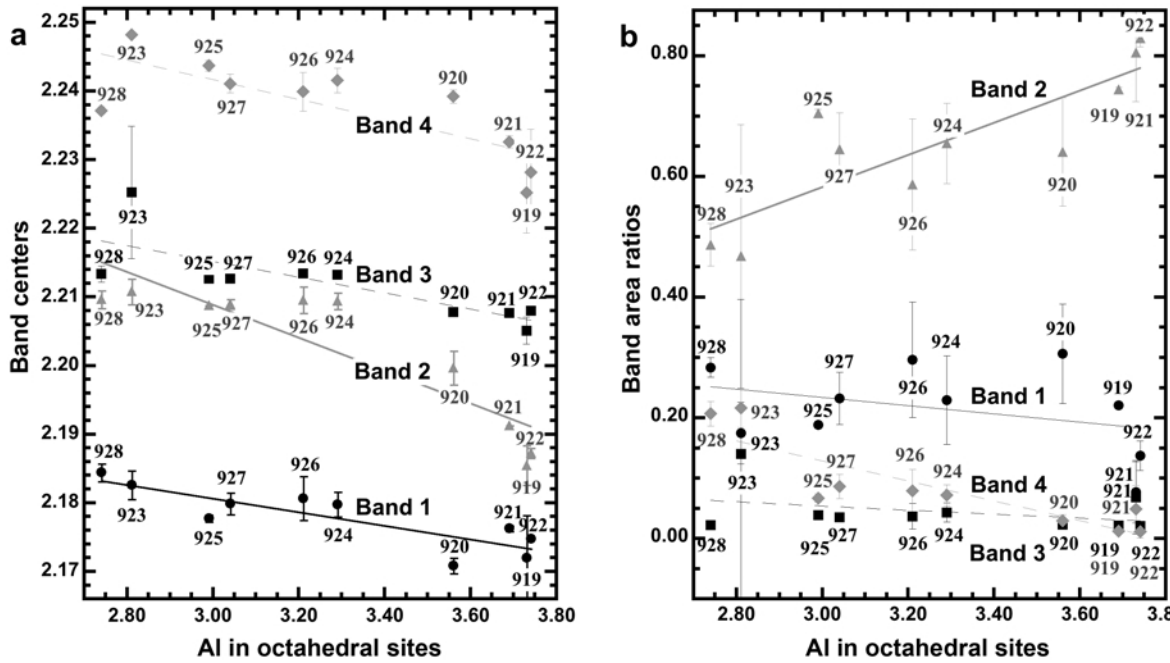

Figure 12. Comparisons of the spectral features with Al abundance in the octahedral sites: (a) band center *vs.* Al; and (b) band area ratios *vs.* Al. These data show the greatest shifts in the band center for band two with varying amounts of substitution for Al in the octahedral sites. Bands one and two have the largest area and show the greatest change in band area with variation in Al in the octahedral sites. Error bars are given from the Gaussian fits. Note that the XRF equivalent value was used for sample JB924 for consistency throughout the analyses.

The wavelength values for the modeled OH combination bands were converted from wavelength to wavenumber (cm^{-1}) for comparison with the OH-bending vibrations. The position of the OH_δ feature near 945 cm^{-1} (10.6 μm) associated with Al_2OH bending in beidellite was used for band 1 for all samples and the position of the OH_δ value near 920 cm^{-1} (10.9 μm) associated with Al_2OH bending in montmorillonite was used for band 2 in all samples. In many cases, obvious bands were observed in the spectra for the fundamental OH_δ bending vibrations (Table 4). In some cases only a shoulder feature was present and the band center was estimated and labeled as a shoulder feature. Band positions were then calculated for the fundamental OH-stretching vibrations based on the modeled OH combination features (bands 1 and 2, which comprised most of the band area). Band 1 resulted in OH_ν values of 3644–3663 cm^{-1} (2.73–2.74 μm) (excluding the spectrum of sample JB928A which had a lower value). Band 2 resulted in estimated OH_ν stretching values of 3603–3656 cm^{-1} (2.74–2.78 μm) for the beidellite samples and 3602–3613 cm^{-1} (2.77–2.78 μm) for the

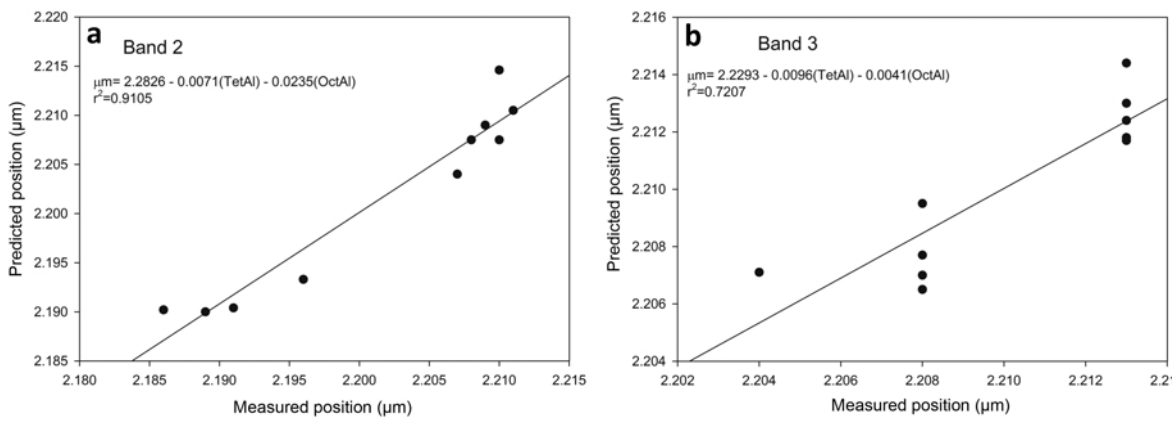

Figure 13. Predicted values for the wavelength of (a) NIR band 2; and (b) NIR band 3 from regression analyses of tetrahedral and octahedral Al^{3+} content on the measured NIR positions of ten beidellite and montmorillonite samples.

https://doi.org/10.1346/CCMN.2011.0590403 Published online by Cambridge University Press

intermediate beidellite/montmorillonite samples. These bands were consistent with the OH_v bands observed in the reflectance spectra in Figure 5b, although separating the OH and H_2O stretching vibrations in this region was difficult due to saturation effects. These estimated bands were generally in line with the measured values of OH-stretching vibrations observed in transmission spectra from previous studies (Farmer, 1974; Post and Borer, 2002; Kloprogge, 2006). Post and Borer (2002) found OH_v bands spanning 3651−3655 and 3630−3636 cm^{-1} (2.736−2.739 and 2.750−2.755 μm) in transmission spectra of a group of natural beidellites, many of them the same samples as those studied here. Transmission spectra of reduced-charge montmorillonites (Li-exchanged and heated) contained OH bands at 3671 and 3639 cm^{-1} (2.724 and 2.748 μm) (Komadel *et al.*, 2005). These beidellite OH values were all higher than the OH_v values typically observed near 3620−3630 cm^{-1} (~2.75−2.76 μm) for Al_2OH sites in transmission spectra of montmorillonites (*e.g.* Farmer, 1974; Madejová *et al.*, 1994; Bishop *et al.*, 2002a).

Another approach was used to estimate the OH_v and $OH_{v+\delta}$ bands as well. The OH-stretching overtone (OH_{2v}) was measured for spectra of both the loose and pressed textures of the samples (Table 5). The beidellites exhibited OH_{2v} bands at 1.399−1.400 μm (7141−7148 cm^{-1}), while the intermediate beidellite/montmorillonites had OH_{2v} bands at 1.411−1.413 μm (7079−7086 cm^{-1}). These overtone values were converted to OH_v values using the method developed by Petit *et al*. (2004) where an anharmonicity constant of −85.6 cm^{-1} is used. The resulting OH_v values (Table 5) of 3656−3659 cm^{-1} (2.733−2.735 μm) for beidellite and 3625−3629 cm^{-1} (2.756−2.759 μm) for beidellite-montmorillonite were consistent with the observed bands in Figure 5b.

Geologic implications of beidellites and beidellite/montmorillonite mixtures in clay systems

Dioctahedral smectites could be indicator minerals for geothermal reservoirs as shown through a study of the montmorillonite–beidellite transition at a geothermal field at Guadeloupe, Lesser Antilles (Guisseau *et al.*, 2007). That study showed that crystallization of montmorillonite occurred where cool (~<100ºC) surface water entered the system, whereas beidellite formed where hot (~110−160ºC) Mg-free fluids entered the system from below. Similar studies (Papapanagiotou *et al.*, 2003) of a geothermal field at Chipilapa, El Salvador, also found montmorillonite formation at the upper part of the sequence (<130ºC) and beidellite formation in deeper, hotter fluids (130−200ºC). Additional montmorillonite to beidellite transitions were observed with increasing depth and temperature of the fluids in other active geothermal systems (Yang *et al.*, 2001; Inoue *et al.*, 2004). An example of montmorillonite and beidellite precipitation is illustrated in Figure 14 where both could be forming in the same geothermal system, but separately such that montmorillonite occurs at the surface where meteoric water infiltrates the system and beidellite occurs where hot fluids ascend from deeper geothermal reservoirs.

Table 5. Measured and calculated band centers.

Sample ID	OH 2ν (μm) Measured	OH 2ν (cm^{-1}) Measured	OH ν (cm^{-1}) Calculated	OH δ Measured	OH ν+δ (cm^{-1}) Calculated
B34 JB919A Delamar	1.4004	7140.8	3656.0	946	4602.0
B34 JB919B Delamar	1.4003	7141.3	3656.3	948	4604.3
B35 JB920A SBId-1	1.3993	7146.4	3658.8	947	4605.8
B35 JB920B SBId-1	1.3995	7145.4	3658.3	949	4607.3
B36 JB921A SBCa-1	1.3998	7143.9	3657.6	941	4598.6
B36 JB921B SBCa-1	1.3997	7144.4	3657.8	945	4602.8
B37 JB922A 3rd bench	1.3991	7147.5	3659.4	942	4601.4
B37 JB922B 3rd bench	1.3991	7147.5	3659.4	946	4605.4
B38 JB923A Cameron	1.4113	7085.7	3628.5	928	4556.5
B38 JB923B Cameron	1.4115	7084.7	3628.0	927	4555.0
B39 JB924A Mt Binjour	1.4115	7084.7	3628.0	928	4556.0
B39 JB924B Mt Binjour	1.4113	7085.7	3628.5	926	4554.5
B40 JB925A BP <0.1	1.4127	7078.6	3624.9	924	4548.9
B40 JB925B BP <0.1	1.4117	7083.7	3627.5	925	4552.5
B41 JB926A BP 0.1−0.2	1.4121	7081.7	3626.5	918	4544.5
B41 JB926B BP 0.1−0.2	1.4117	7083.7	3627.5	926	4553.5
B42 JB927A BP 0.2−0.5	1.4121	7081.7	3626.5	918	4544.5
B42 JB927B BP 0.2−0.5	1.4121	7081.7	3626.5	926	4552.5
B43 JB928A BP 0.5−2.0	1.4123	7080.6	3625.9	923	4548.9
B43 JB928B BP 0.5−2.0	1.4123	7080.6	3625.9	922	4547.9

$OH_{v+\delta}$ = OH stretching plus bending combination band; OH_v = OH stretching vibration; OH_δ = OH bending vibration.

https://doi.org/10.1346/CCMN.2011.0590403 Published online by Cambridge University Press

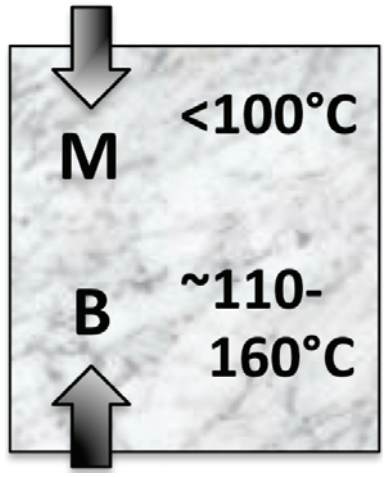

Figure 14. Diagram of possible beidellite formation: beidellite (B) generally precipitates from geothermal fluids entering a system from below, while montmorillonite (M) normally forms at lower temperatures, often where cool water enters the system from above.

Alternatively, a transition from montmorillonite to beidellite could occur during the initial phase of illitization as observed in burial diagensis (Saito *et al.*, 2003). Beidellite formation occurred gradually through a mechanism of Al substitution for Si in a solid-state process. This transformation mechanism is supported by laboratory experiments where montmorillonite was converted to beidellite and illite over the temperature range 100−200ºC (Beaufort *et al.*, 2001). Beidellite is frequently mixed with montmorillonite in soil smectites (Wilson, 1987) and has occurred as an intermediary in the formation of mixed-layer illite/montmorillonite from montmorillonite (observed as regions of increased tetrahedral substitution of Al-for-Si in montmorillonite) (Frank-Kamenetski *et al.*, 1979). In addition, the temperature sensitivity of *cis*-vacant and *trans*-vacant sites in beidellite may be related to the transformation of montmorillonite to illite *via* beidellite (Lantenlois *et al.*, 2008). Study of illitization of montmorillonite suggests formation of triple-layer type materials where a normal low-charge montmorillonite unit is surrounded by high-charge vermiculite or beidellite-type units above and below that are then neighboring illite-type units (Meunier *et al.*, 2000). These studies together support the process of montmorillonite alteration to beidellite then illite and chlorite (Guisseau *et al.*, 2007). Other illitization studies have also observed transformations from beidellite to illite then muscovite rather than chlorite (*e.g.* Gharrabi *et al.*, 1998; Drief and Nieto, 2000; Meunier and Velde, 2004). These studies also suggest the presence of mixed-layer illite-smectite and illite as end-member species for temperatures below ~360ºC. Thermal experiments have also shown that beidellite is more stable than montmorillonite or intermediate beidellite/montmorillonite samples at elevated temperatures (Yamada *et al.*, 1991; Yamada and Nakazawa, 1993).

Importance for Mars

Beidellites have been suggested as a possible phyllosilicate present on Mars through analyses of hyperspectral CRISM data in the Mawrth Vallis region (Noe Dobrea *et al.*, 2010). The reflectance spectra of some surface units in the Libya Montes and Nili Fossae regions may be consistent with the presence of beidellite. Identifying locations of beidellite *vs.* montmorillonite on Mars is important because these Al-rich smectites form under different geologic conditions (Papanastassiou and Wasserburg, 1974; Guisseau *et al.*, 2007) and may thus be able to provide information about the ancient geologic history of Mars.

Beidellite outcrops have been observed in CRISM images of the Libya Montes, Nili Fossae, and Mawrth Vallis regions of Mars (Figure 15). The Libya Montes scene from image FRT0000B0CB (Figure 15b) is dominated by mafic rock and sand but has a small outcrop of clay-bearing material with spectral characteristics of beidellite. The strongest beidellite signature in the image is indicated by the arrow. Al-rich clays are rare in this region and spectra consistent with montmorillonite have not yet been observed. The most common clay signatures detected are consistent with Fe/Mg-smectite that may be accompanied by carbonate in some regions (Bishop *et al.*, 2010). These Fe/Mg-smectite outcrops are found only in the ancient Noachian rocks that have been exposed underneath olivine- and pyroxene-bearing material. The Libya Montes region is similar to the Nili Fossae region nearby, where larger clay outcrops have been detected using the Observatoire pour la Minéralogie, l'Eau, les Glaces et l'Activité (OMEGA) spectrometer on Mars Express (Poulet *et al.*, 2005) as well as CRISM (Mustard *et al.*, 2008; Ehlmann *et al.*, 2009). Illite, chlorite, and prehnite have been detected in the Nili Fossae region and hydrothermal processes are thought to have occurred there, but montmorillonite has not yet been identified (Ehlmann *et al.*, 2009). However, beidellite may be present at Nili Fossae as well (Figure 15c). Phyllosilicate outcrops marked by 1 and 2 (Figure 15c) are consistent with mixtures of prehnite and beidellite, where type 1 exhibits stronger prehnite signatures and type 2 exhibits stronger beidellite signatures. The presence of beidellite and apparent absence of montmorillonite at Libya Montes and Nili Fossae could indicate a hydrothermal origin of this Al smectite in outcrops surrounding the Isidis impact basin.

The Mawrth Vallis region, in contrast to Libya Montes, contains a wealth of clays, both Fe/Mg rich and Al rich that have been identified using hyperspectral images collected by OMEGA (Poulet *et al.*, 2005; Loizeau *et al.*, 2007) and CRISM (Bishop *et al.*, 2008b; Mustard *et al.*, 2008; McKeown *et al.*, 2009; Noe Dobrea *et al.*,

https://doi.org/10.1346/CCMN.2011.0590403 Published online by Cambridge University Press

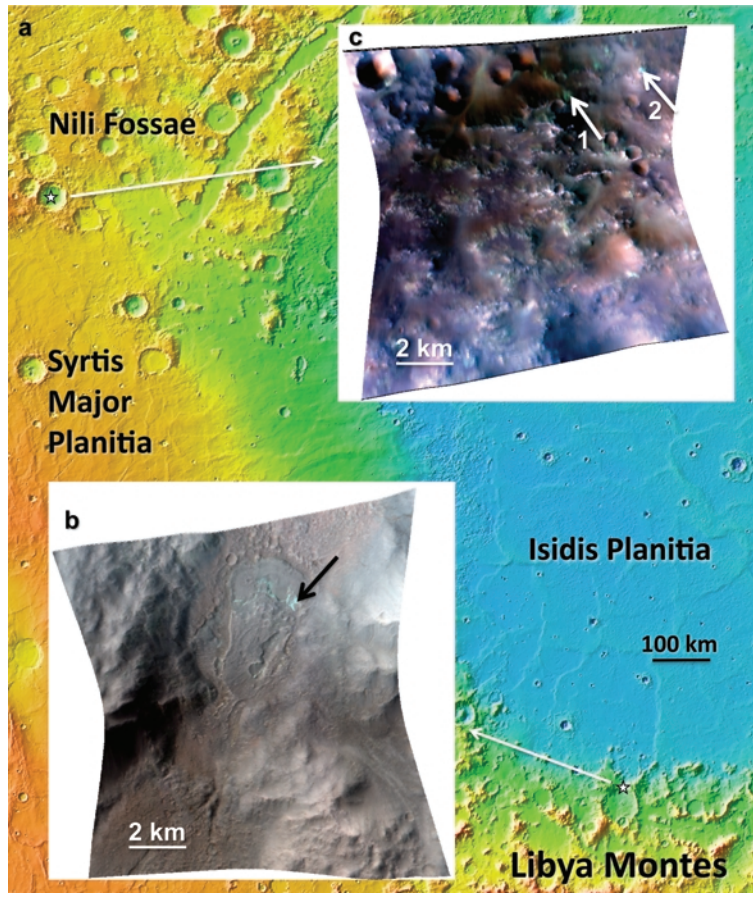

Figure 15 (*a–c above, d,e facing page*). Beidellite outcrops in CRISM images with Mars Orbiter Laser Altimer (MOLA) data for context on Mars: (a) MOLA image of Isidis Planitia region; (b) FRT0000B0CB from Libya Montes; (c) FRT0000454E from Nili Fossae; (d) MOLA image of Mawrth Vallis region; and (e) HRL000043EC from Mawrth Vallis. The strongest beidellite occurrences are marked by the arrows. Al phyllosilicates are rare in the Libya Montes region. This beidellite outcrop occurs as a single clay unit among basaltic rocks. Small isolated phyllosilicate outcrops occur in this Nili Fossae image, where site 1 is a mixture of prehnite and beidellite dominated by prehnite and site 2 is a similar mixture dominated by beidellite. In contrast, the Mawrth Vallis region contains multiple, large outcrops of phyllosilicate-rich material including an upper unit spectrally dominated by Al smectites, hydrated silica, and kaolinite. The arrow marks the region of intermediate beidellite/ montmorillonite smectite.

2010). The Fe/Mg smectite unit is 100–200 m thick and is covered by a thinner 10–40 m thick unit of Al phyllosilicates (Wray *et al.*, 2008; Loizeau *et al.*, 2010). The Al phyllosilicate unit was observed to contain montmorillonite, kaolinite, and hydrated silica (Bishop *et al.*, 2008b), and more recently beidellite was also reported (Noe Dobrea *et al.*, 2010). Clay signatures are present in about one third of CRISM image HRL00043EC over Mawrth Vallis (Figure 15e), where Al smectite spectral signatures are observed. An outcrop with an example of an intermediate beidellite/montmorillonite signature is marked by the arrow. Pockets of such beidellite/montmorillonite materials in a region of montmorillonite-type material could indicate that higher-temperature alteration occurred in some regions.

The CRISM ratio spectra of the regions marked in Figure 15 were compared with lab reflectance spectra of a beidellite and intermediate beidellite montmorillonite sample (Figures 16, 17). The clay signatures found in these regions on Mars exhibit absorption features near 1.4, 1.9, and 2.2 μm that are consistent with spectra of Al-rich smectites (Bishop *et al.*, 1994); variation in the position of the band centered at 2.2 μm was observed, consistent with the presence of intermediate beidellite/montmorillonites and montmorillonite, as presented in Figure 6 and previous studies (Post and Noble, 1993; Gates, 2005). In some cases the exact position of the 1.4 μm band in the CRISM spectra does not match perfectly with the positions observed in laboratory spectra of intermediate beidellite/montmorillonites, but this feature is often very weak and not as reliable for phyllosilicate detection as the 2.2–2.3 μm region in CRISM spectra.

The Al smectite spectrum (Figure 16) from Libya Montes (Figure 15b) contains a band centered near 2.18 μm which is most consistent with beidellite, whereas the corresponding band in the spectrum from

https://doi.org/10.1346/CCMN.2011.0590403 Published online by Cambridge University Press

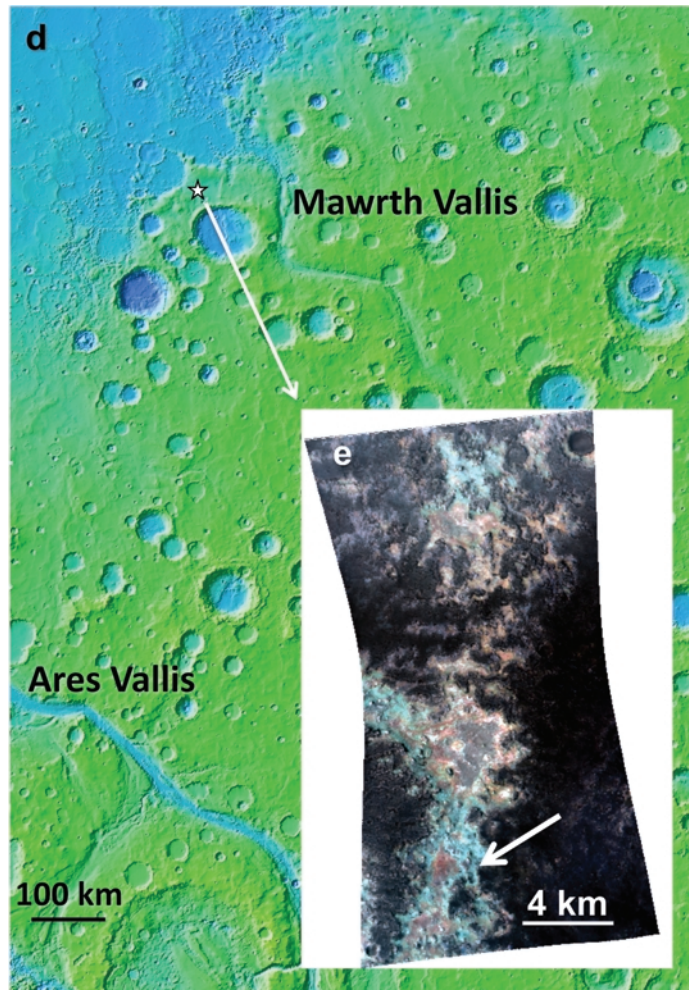

(Figure 16) Mawrth Vallis (Figure 15e) is broader and asymmetric, with a minimum near 2.205 and a shoulder near 2.18 μm, which is most consistent with an intermediate beidellite/montmorillonite. Each of these spectra includes a band near 1.9 μm typical of interlayer water in smectites, plus a band near 1.4 μm due to both the Al_2OH stretching overtone (1.40 μm in beidellite and 1.41 μm in montmorillonite) and the H_2O stretch plus two bend combination (1.41 μm). The Al smectite signature in the Libya Montes scene is weaker than that observed at Mawrth Vallis, probably because a lesser abundance of smectite is present at Libya Montes. The band center at 1.4 μm for this outcrop is broadened but does not match perfectly the lab spectra of beidellites; this may be due to admixtures or noise in the spectra.

Spectra of two phyllosilicate outcrops from Nili Fossae image FRT0000454E were compared to lab spectra of beidellite, intermediate beidellite/montmorillonite, and prehnite (Figure 17). The Nili Fossae-1 spectrum exhibits stronger bands near 1.48 and 2.36 μm that are characteristic of prehnite, whereas the Nili Fossae-2 spectrum exhibits stronger features near 1.4 and 2.19 μm that are consistent with beidellite. Spectra from related outcrops in this image were reported by Ehlmann *et al.* (2009) to contain mixtures of illite, chlorite, and prehnite; however, mixtures of beidellite and prehnite were found to be better matches to the spectra reported in the present study.

CONCLUSIONS

The spectral reflectance properties of Al-rich smectites included measurable differences for beidellites (greater tetrahedral charge than octahedral charge) and montmorillonites (greater octahedral charge than tetrahedral charge). The study of ten beidellites and intermediate beidellite/montmorillonites summarized the differences in their spectral signatures. The Al_2OH stretching overtone was observed at 1.399–1.400 μm (7141–7148 cm^{-1}) for beidellite and at 1.411–1.413 μm (7079–7086 cm^{-1}) for intermediate beidellite/montmorillonite smectites. The

https://doi.org/10.1346/CCMN.2011.0590403 Published online by Cambridge University Press

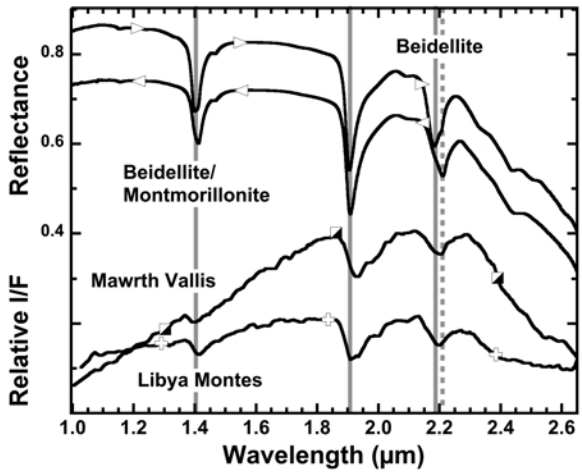

Figure 16. Relative CRISM I/F spectra from 1 to 2.65 μm of beidellite outcrops in Libya Montes and Mawrth Vallis compared with lab reflectance spectra of beidellite (JB921A) and beidellite/montmorillonite (JB927A). The Libya Montes spectrum is a 3×3 pixel spot centered at x228 y367 (non-projected) ratioed to a spectrally unremarkable region of the same size in the same column from image FRT0000B0CB, version TRR3. The Mawrth Vallis spectrum is a 10×10 pixel spot centered at x186 y505 (non-projected) from image HRL000043EC, version TRR2, also ratioed to a spectrally unremarkable region in the scene. The CRISM spectra were treated with a 2- (Libya Montes) or 3- (Mawrth Vallis) point sliding window smoothing routine to reduce noise. The Libya Montes spectrum more closely resembles the lab spectra of beidellite, while the Mawrth Valles spectrum is more consistent with the beidellite/montorillonite lab spectra.

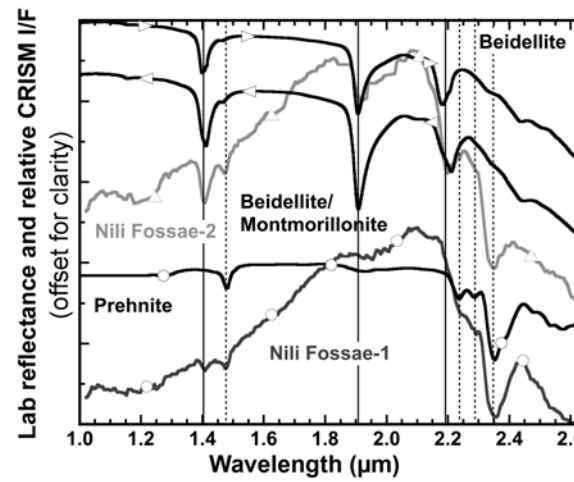

Figure 17. Relative CRISM I/F spectra from 1 to 2.65 μm of phyllosilicate outcrops in Nili Fossae image FRT0000454E, version TRR3. The projected image was ratioed to a 10×10 spot centered at x255 y370, then spectra were collected from this image at 5×5 pixel spots centered at x437 y135 and x572 y86. These were compared with lab reflectance spectra of beidellite (JB921A) and beidellite/montmorillonite (JB927A) from this study, and USGS prehnite (GDS613) from http://speclab.cr.usgs.gov/spectral-lib.html. The CRISM spectra were treated with a 2-point sliding window smoothing routine to reduce noise. Both spectra are consistent with mixtures of beidellite and prehnite. The Nili Fossae-1 spectrum has stronger prehnite features, while the Nili Fossae-2 spectrum has stronger beidellite features.

Al_2OH stretch plus bend combination band was observed near 2.18 μm (4587 cm^{-1}) for beidellite and near 2.21 μm (4525 cm^{-1}) with an additional band or shoulder near 2.18 μm (4587 cm^{-1}) for intermediate beidellite/montmorilonites. Beidellite spectra also exhibited weaker bands near 2.34 and 2.44 μm (~4275 and ~4100 cm^{-1}), whereas reflectance spectra of montmorillonite exhibit a weak band near 2.45 μm (~4080 cm^{-1}). The Al_2OH bending vibrations were observed near 941–948 cm^{-1} (10.5–10.6 μm) in the beidellite spectra and near 918–926 cm^{-1} (10.8–10.9 μm) in the montmorillonite and intermediate beidellite/montmorillonite spectra. Shifts were also observed in the Si–O–Al bending vibrations from 552 and 480 cm^{-1} (18.1 and 20.8 μm) for beidellite spectra to 544 and 475 cm^{-1} (18.4 and 21.0 μm) in montmorillonite spectra.

Gaussian modeling of the 2.2 μm (~4545 cm^{-1}) combination band region for ten beidellite and beidellite/montmorillonite spectra resulted in four overlapping bands attributed to OH combination bands in beidellite and montmorillonite. The wavelength position of the band center and area ratios of these four bands resulting from the Gaussian modeling generally exhibited consistent trends associated with the octahedral and tetrahedral cation compositions of the beidellites, intermediate beidellite/montmorillonites, and montmorillonite samples studied.

The VNIR Al smectite reflectance spectra described here were compared with the Al smectite type reflectance spectra observed in two locations on Mars. A spectrum with a 2.19 μm (4566 cm^{-1}) band consistent with beidellite was observed in an isolated Al phyllosilicate-bearing outcrop in Libya Montes. Reflectance spectra consistent with beidellite were also found in the Nili Fossae region. Both of these regions border the Isidis Basin and are thought to have experienced hydrothermal alteration (Ehlmann *et al.*, 2009; Mustard *et al.*, 2009). A reflectance spectrum more similar to the intermediate beidellite/montmorillonite samples was observed in one location in Mawrth Vallis, a region dominated by thick Fe/Mg smectite units covered by thin units of montmorillonite, other Al phyllosilicates, and hydrated silica (Bishop *et al.*, 2008). Based on the lower-temperature formation conditions typical of montmorillonite and higher-temperature formation conditions typical of beidellite, detections of these Al smectites on Mars could act as geothermometers or indicators of alteration conditions.

ACKNOWLEDGMENTS

Support of this study from the Mars Fundamental Research program, the MRO mission, and NASA's

Graduate Student Researcher's program are much appreciated. The authors thank M. Raven and P. Self (CSIRO) for the X-ray analyses and are also grateful to P. Self, J. Michalski, B. Ehlmann, R. Milliken, and J. Stucki for helpful comments which improved the manuscript. Smectech (Australia) provided funds for chemical analyses. Brown University's RELAB is supported by NASA grant NNG06GJ31G.

REFERENCES

Anderson, J.H. and Wickersheim, K.A. (1964) Near infrared characterization of water and hydroxyl groups on silica surfaces. *Surface Science*, **2**, 252–260.

Battaglia, S., Leoni, L., and Sartori, F.A. (2006) A method for determining the CEC and chemical composition of clays via XRF. *Clay Minerals*, **41**, 717–725.

Beaufort, D., Berger, G., Lacharpagne, J.C., and Meunier, A. (2001) An experimental alteration of montmorillonite to a di + trioctahedral smectite assemblage at 100 and 200ºC. *Clay Minerals*, **36**, 211–225.

Besson, G. and Drits, V.A. (1997a) Refined relationships between chemical composition of dioctahedral fine-grained micaceous minerals and their infrared spectra within the OH stretching region. Part I: Identification of the OH stretching bands. *Clays and Clay Minerals*, **45**, 158–169.

Besson, G. and Drits, V.A. (1997b) Refined relationships between chemical composition of dioctahedral fine-grained micaceous minerals and their infrared spectra within the OH stretching region. Part II: The main factors affecting OH vibrations and quantitative analysis. *Clays and Clay Minerals*, **45**, 170–183.

Bishop, J.L., Pieters, C.M., and Burns, R.G. (1993) Reflectance and Mössbauer spectroscopy of ferrihydrite-montmorillonite assemblages as Mars soil analog materials. *Geochimica et Cosmochimica Acta*, **57**, 4583–4595.

Bishop, J.L., Pieters, C.M., and Edwards, J.O. (1994) Infrared spectroscopic analyses on the nature of water in montmorillonite. *Clays and Clay Minerals*, **42**, 701–715.

Bishop, J.L., Madejová, J., Komadel, P., and Fröschl, H. (2002a) The influence of structural Fe, Al and Mg on the infrared OH bands in spectra of dioctahedral smectites. *Clay Minerals*, **37**, 607–616.

Bishop, J.L., Murad, E., and Dyar, M.D. (2002b) The influence of octahedral and tetrahedral cation substitution on the structure of smectites and serpentines as observed through infrared spectroscopy. *Clay Minerals*, **37**, 617–628.

Bishop, J.L., Lane, M.D., Dyar, M.D., and Brown, A.J. (2008a) Reflectance and emission spectroscopy study of four groups of phyllosilicates: Smectites, kaolinite-serpentines, chlorites and micas. *Clay Minerals*, **43**, 35–54.

Bishop, J.L., Noe Dobrea, E.Z., McKeown, N.K., Parente, M., Ehlmann, B.L., Michalski, J.R., Milliken, R.E., Poulet, F., Swayze, G.A., Mustard, J.F., Murchie, S.L., and Bibring, J.-P. (2008b) Phyllosilicate diversity and past aqueous activity revealed at Mawrth Vallis, Mars. *Science*, **321**, DOI: 10.1126/science.1159699, pp. 830–833.

Bishop, J.L., Makarewicz, H.D., Perry, K.A., McKeown, N.K., Parente, M., Tornabene, L.L., Swayze, G.A., Clark, R.N., Mustard, J.F., Murchie, S.L., and McEwen, A.S. (2010) Mineralogy of the Libya Montes and the Southern Isidis Planitia region: CRISM detection of clay, carbonate, olivine and pyroxene, and correlation with HiRISE imagery. *Lunar and Planetary Science Conference*, abstract #2147.

Bodine, M.W., Jr. (1987) CLAYFORM: A Fortran 77 computer program apportioning the constituents in the chemical analysis of a clay or other silicate mineral in a structural formula. *Computers and Geosciences*, **13**, 77–88.

Brindley, G.W. and Brown, G. (1980) *Crystal Structures of Clay Minerals and their X-ray Identification.* Mineralogical Society, London, 495 pp.

Chamley, H. (1989) *Clay Sedimentology.* Springer-Verlag, New York, 623 pp.

Drief, A. and Nieto, F. (2000) Chemical composition of smectites formed in clastic sediments. Implications for the smectite-illite transformation. *Clay Minerals*, **35**, 665–678.

Ehlmann, B.L., Mustard, J.F., Swayze, G.A., Clark, R.N., Bishop, J.L., Poulet, F., Marais, D.J.D., Roach, L.H., Milliken, R.E., Wray, J.J., Barnouin-Jha, O. and Murchie, S.L. (2009) Identification of hydrated silicate minerals on Mars using MRO-CRISM: Geologic context near Nili Fossae and implications for aqueous alteration. *Journal of Geophysical Research*, **114**, doi:10.1029/2009JE003339.

Farmer, C.B., Davies, D.W., Holland, A.L., LaPorte, D.D., and Doms, P.E. (1977) Mars: Water vapor observations from the Viking orbiters. *Journal of Geophysical Research*, **82**, 4225–4248.

Farmer, V.C. (1974) The layer silicates. Pp. 331–363 in: *The Infrared Spectra of Minerals* (V.C. Farmer, editors). Monograph **4**. The Mineralogical Society, London.

Frank-Kamenetski, V.A., Kotelnikova, E.N., Kotov, N.V., and Starke, R. (1979) Influence of tetrahedral aluminium on the hydrothermal transformation of montmorillonite and beidellite to mixed-layer illite-montmorillonite and illite. *Kristall und Technik*, **14**, 303–311. Wiley-VCH Verlag GmbH and Co. KGaA, Weinheim, Germany.

Gates, W.P. (2005) Infrared spectroscopy and the chemistry of dioctahedral smectites. Pp. 125–168 in: *The Application of Vibrational Spectroscopy to Clay Minerals and Layered Double Hydroxides* (J.T. Kloprogge, editors). The Clay Minerals Society, Colorado, USA.

Gates, W.P., Komadel, P., Madejová, J., Bujdák, J., Stucki, J.W., and Kirkpatrick, R.J. (2000) Electronic and structural properties of reduced-charge montmorillonites. *Applied Clay Science*, **16**, 257–271.

Gates, W.P., Slade, P.G., Lanson, B., and Manceau, A. (2002) Site occupancies by iron in nontronites. *Clays and Clay Minerals*, **50**, 223–239.

Gharrabi, M., Velde, B., and Sagon, J.-P. (1998) The transformation of illite to muscovite in pelitic rocks: Constraints from X-ray diffraction. *Clays and Clay Minerals*, **46**, 79–88.

Grauby, O., Petit, S., Decarreau, A., and Baronnet, A. (1993) The beidellite-saponite series: An experimental approach. *European Journal of Mineralogy*, **5**, 623–635.

Grim, R.E. (1968) *Clay Mineralogy.* McGraw-Hill Book Co., New York, 596 pp.

Guisseau, D., Mas, P.P., Beaufort, D., Girard, J.P., Inoue, A., Sanjuan, B., Petit, S., Lens, A., and Genter, A. (2007) Sigificance of the depth-related transition montmorillonite-beidellite in the Bouillante geothermal field (Guadeloupe, Lesser Antilles). *American Mineralogist*, **92**, 1800–1813.

Hiroi, T. and Pieters, C.M. (1998) Modified Gaussian deconvolution of reflectance spectra of Lunar soils. *Lunar and Planetary Science Conference*, abstract #1253.

Hunt, G.R. and Salisbury, J.W. (1970) Visible and near-infrared spectra of minerals and rocks: 1. Silicate minerals. *Modern Geology*, **1**, 283–300.

Inoue, A., Meunier, A., and Beufort, D. (2004) Illite-smectite mixed-layer minerals in felsic volcaniclastic rocks from drill cores, Kakkonda, Japan. *Clays and Clay Minerals*, **52**, 66–84.

Kloprogge, J.T. (2006) Spectroscopic studies of synthetic and natural beidellites: A review. *Applied Clay Science*, **31**, 165–179.

Kloprogge, J.T., Komarneni, S., Yanagisawa, K., Frost, R.L., and Fry, R. (1998) Infrared study of some synthetic and natural beidellites. *Journal of Materials Science Letters*, **17**,

1853–1855.
Komadel, P., Madejová, J., and Bujdák, J. (2005) Preparation and properties of reduced-charge smectites – A review. *Clays and Clay Mineral*, **53**, 313–334.
Lanson, B. and Champion, D. (1991) The I/S-to-illite reaction in the late stafe diagenesis. *American Journal of Science*, **291**, 473–506.
Lanson, B. and Besson, G. (1992) Characterization of the end of smectite-to-illite transformation: Decomposition of X-ray patterns. *Clays and Clay Minerals*, **40**, 40–52.
Lantenlois, S., Muller, F., Bény, J.-M., Mahiaoui, J., and Champallier, R. (2008) Hydrothermal synthesis of beidellites: Characterization and study of the cis- and trans-vacant character. *Clays and Clay Minerals*, **56**, 39–48.
Larsen, E.S. and Wherry, E.T. (1925) Beidellite, a new mineral name. *Journal of the Washington Academy of Sciences*, **15**, 465–466.
Loizeau, D., Mangold, N., Poulet, F., Bibring, J.-P., Gendrin, A., Ansan, V., Gomez, C., Gondet, B., Langevin, Y., Masson, P., and Neukum, G. (2007) Phyllosilicates in the Mawrth Vallis region of Mars. *Journal of Geophysical Research*, **112**, doi:10.1029/2006JE002877.
Loizeau, D., Mangold, N., Poulet, F., Ansan, V., Hauber, E., Bibring, J.P., Gondet, B., Langevin, Y., Masson, P., and Neukum, G. (2010) Stratigraphy in the Mawrth Vallis region through OMEGA, HRSC color imagery and DTM. *Icarus*, **205**, 396–418.
Madejová, J., Komadel, P., and Cicel, B. (1994) Infrared study of octahedral site populations in smectites. *Clay Minerals*, **29**, 319–326.
Madejová, J., Bujdak, J., Gates, W.P., and Komadel, P. (1996) Preparation and infrared spectroscopic characterization of reduced-charge montmorillonite with various Li contents. *Clay Minerals*, **31**, 233–241.
Makarewicz, H.D., Parente, M., and Bishop, J.L. (2009) Deconvolution of VNIR Spectra Using Modified Gaussian Modeling (MGM) with Automatic Parameter Initialization (API) Applied to CRISM. In Hyperspectral Image and Signal Processing: Evolution in Remote Sensing. IEEE: WHISPERS, pp. doi: 10.1109/WHISPERS.2009.5289046 IEEE.
Malla, P.B. and Douglas, L.A. (1987) Problems in identification of montmorillonite and beidellite. *Clays and Clay Minerals*, **35**, 232–236.
McKeown, N.K., Bishop, J.L., Noe Dobrea, E.Z., Ehlmann, B.L., Parente, M., Mustard, J.F., Murchie, S.L., Swayze, G.A., Bibring, J.-P., and Silver, E. (2009) Characterization of phyllosilicates observed in the central Mawrth Vallis region, Mars, their potential formational processes, and implications for past climate. *Journal of Geophysical Research*, **114**, doi:10.1029/2008JE003301.
McKeown, N.K., Bishop, J.L., Cuadros, J., Hillier, S., Amador, E., Makarewicz, H.D., Parente, M., and Silver, E. (2011) Interpretation of reflectance spectra of mixtures of clay minerals and silica: implications for Martian clay mineralogy at Mawrth Vallis. *Clays and Clay Minerals*, **59**, typesetter, pls add page numbers.
Meunier, A. and Velde, B. (2004) *Illite: Origins, Evolution and Metamorphism.* Springer Verlag, Berlin, 286 pp.
Meunier, A., Lanson, B., and Beaufort, D. (2000) Vermiculitization of smectite interfaces and illite layer growth as a possible dual model for illite-smectite illitization in diagenetic environments: a synthesis *Clay Minerals*, **35**, 573–586.
Michalski, J.R., Kraft, M.D., Sharp, T.G., Williams L.B., and Christensen, P.R. (2005) Emission spectroscopy and crystal chemistry of smectites: Mineralogical constraints on the high-silica Martian surface component observed by TES. *Icarus*, **174**, 161–171.
Milliken, R.E., Swayze, G.A., Arvidson, R.L., Bishop, J.L., Clark, R., Ehlmann, B.L., Grotzinger, J., Morris, R., Murchie, S., Mustard, J., and Weitz, C. (2008a) Spectral evidence for sedimentary silica on Mars. *Lunar and Planetary Science XXXIX*, abstract #2025.
Milliken, R.E., Swayze, G.A., Arvidson, R.E., Bishop, J.L., Clark, R.N., Ehlmann, B.L., Green, R.O., Grotzinger, J., Morris, R.V., Murchie, S.L., Mustard, J.F., and Weitz, C.M. (2008b) Opaline silica in young deposits on Mars. *Geology*, **36**, 847–850; doi: 10.1130/G24967A.1.
Murchie, S., Arvidson, R., Bedini, P., Beisser, K., Bibring, J.-P., Bishop, J., Boldt, J., Cavender, P., Choo, T., Clancy, R.T., Darlington, E.H., Des Marais, D., Espiritu, R., Fort, D., Green, R., Guinness, E., Hayes, J., Hash, C., Heffernan, K., Hemmler, J., Heyler, G., Humm, D., Hutcheson, J., Izenberg, N., Lee, R., Lees, J., Lohr, D., Malaret, E., Martin, T., McGovern, J.A., McGuire, P., Morris, R., Mustard, J., Pelkey, S., Rhodes, E., Robinson, M., Roush, T., Schaefer, E., Seagrave, G., Seelos, F., Silvergate, P., Slavney, S., Smith, M., Shyong, W.-J., Strohbehn, K., Taylor, H., Thompson, P., Tossman, B., Wirzburger, M., and Wolff, M. (2007) Compact Reconnaissance Imaging Spectrometer for Mars (CRISM) on Mars Reconnaissance Orbiter (MRO). *Journal of Geophysical Research*, **112**, doi:10.1029/2006JE002682.
Murchie, S.L., Mustard, J., Ehlmann, B., Milliken, R.E., Bishop, J., McKeown, N., Noe Dobrea, E., Seelos, F., Buczkowski, D., Wiseman, S., Arvidson, R., Wray, J., Swayze, G., Clark, R., Des Marais, D., McEwen, A., and Bibring, J.-P. (2009) A synthesis of Martian aquous mineralogy after 1 Mars year of observations from the Mars Reconnaissance Orbiter. *Journal of Geophysical Research*, **114**, E00D06, doi:10.1029/2009JE003342.
Mustard, J.F., Murchie, S.L., Pelkey, S.M., Ehlmann, B.L., Milliken, R.E., Grant, J.A., Bibring, J.-P., Poulet, F., Bishop, J.L., Noe Dobrea, E.Z., Roach, L.A., Seelos, F., Arvidson, R.E., Wiseman, S., Green, R., Hash, C., Humm, D., Malaret, E., McGovern, J.A., Seelos, K., Clancy, R.T., Clark, R.N., Des Marais, D., Izenberg, N., Knudson, A.T., Langevin, Y., Martin, T., McGuire, P., Morris, R.V., Robinson, M., Roush, T., Smith, M., Swayze, G.A., Taylor, H., Titus, T.N., and Wolff, M. (2008) Hydrated silicate minerals on Mars observed by the Mars Reconnaissance Orbiter CRISM instrument. *Nature*, **454**, doi: 10.1038/nature07097, 305–309.
Noble, S.K., Pieters, C.M., Hiroi, T., and Taylor, L.A. (2006) Using the modified Gaussian model to extract quantitative data from lunar soils. *Journal of Geophysical Research*, **111**, doi:10.1029/2006JE002721.
Noe Dobrea, E.Z., Bishop, J.L., McKeown, N.K., Fu, R., Rossi, C.M., Michalski, J.R., Heinlein, C., Hanus, V., Poulet, F., Arvidson, R., Mustard, J.F., Ehlmann, B.L., Murchie, S., McEwen, A.S., Swayze, G., Bibring, J.-P., Malaret, J.F.E., and Hash, C. (2010) Mineralogy and stratigraphy of phyllosilicate-bearing and dark mantling units in the greater Mawrth Vallis: Constraints on geological origin. *Journal of Geophysical Research*, **115**, doi:10.1029/2009JE003351.
Norrish, K. and Hutton, J.T. (1967) An accurate X-ray spectrographic method for the analysis of a wide range of geological samples. *Geochimica et Cosmochimica Acta*, **33**, 431–453.
Papanastassiou, D.A. and Wasserburg, G.J. (1974) Evidence for later formation and young metamorphism in the achondrite Nakhla. *Geophysical Research Letters*, **1**, 23–26.
Papapanagiotou, P., Beaufort, D., Patrier, P., and Traineau, H. (2003) Clay mineralogy of the >0.2 m rock formation of the M1 drill hole of the geothermal field of Milos (Greece). *Bulletin of the Geological Society of Greece*, **28**, 575–586.
Parente, M., Makarewicz, H.D., and Bishop, J.L. (2011)

Decomposition of mineral absorption bands using nonlinear least squares curve fitting: Applications to Martian meteorites and CRISM data. *Planetary and Space Science*, **59**, 423–442.

Petit, S., Decarreau, A., Martin, F., and Buchet, R. (2004) Refined relationship between the position of the fundamental OH stretching and the first overtones for clays. *Physics and Chemistry of Minerals*, **31**, 585–592.

Post, J.L. and Noble, P.N. (1993) The near-infrared combination band frequencies of dioctahedral smectites, micas, and illites. *Clays and Clay Minerals*, **41**, 639–644.

Post, J.L. and Borer, L. (2002) Physical properties of selected illites, beidellites and mixed-layer illite-beidellites from southwestern Idaho, and their infrared spectra. *Applied Clay Science*, **22**, 77–91.

Poulet, F., Bibring, J.-P., Mustard, J.F., Gendrin, A., Mangold, N., Langevin, Y., Arvidson, R.E., Gondet, B., and Gomez, C. (2005) Phyllosilicates on Mars and implications for the early Mars history. *Nature*, **438**, 632–627.

Robert, J.-L. and Kodama, H. (1988) Generalization of the correlations between hydroxyl-stretching wavenumbers and composition of micas in the system K_2O-MgO-Al_2O_3-SiO_2-H_2O: A single model for trioctahedral and dioctahedral micas. *American Journal of Science*, **288A**, 196–212.

Russell, J.D. and Fraser, A.R. (1994) Infrared methods. Pp. 11–67 in: *Clay Mineralogy: Spectroscopic and Chemical Determinative Methods* (M.J. Wilson, editor). Chapman & Hall, London.

Saito, M.A., Sigman, D.M., and Morel, F.M.M. (2003) The bioinorganic chemistry of the ancient ocean: The co-evolution of cyanobacterial metal requirements and biogeochemical cycles at the Archean-Proterozoic boundary? *Inorganic Chimica Acta*, **356**, 308–318.

Salisbury, J.W., Walter, L.S., Vergo, N., and D'Aria, D.M. (1991) *Infrared (2.1–25 μm) Spectra of Minerals.* Johns Hopkins University Press, Baltimore, Maryland, USA, 267 pp.

Salisbury, J.W. and Wald, A. (1992) The role of volume scattering in reducing spectral contrast of reststrahlen bands in spectra of powdered minerals. *Icarus*, **96**, 121–128.

Salisbury, J.W. (1993) Mid-infrared spectroscopy: Laboratory data. Pp. 79–98 in: *Remote Geochemical Analysis: Elemental and Mineralogical Composition* (C.M. Pieters and P.A.J. Englert, editors). Cambridge University Press, Cambridge, UK.

Schultz, L.G. (1969) Lithium and Potassium absorption, dehydroxylation temperature, and structural water content of aluminous smectites. *Clays and Clay Minerals*, **17**, 115–149.

Stubican, V. and Roy, R. (1961) Isomorphous substitution and infra-red spectra of the layer lattice silicates. *American Mineralogist*, **46**, 32–51.

Sunshine, J.M. and Pieters, C.M. (1993) Estimating modal abundances from the spectra of natural and laboratory pyroxene mixtures using the Modified Gaussian Model. *Journal of Geophysical Research*, **98**, 9075–9087.

Sunshine, J.M., Pieters, C.M., and Pratt, S.F. (1990) Deconvolution of mineral absorption bands: An improved approach. *Journal of Geophysical Research*, **95**, 6955–6966.

Velde, B. (1995) *Origin and Mineralogy of Clays.* Springer-Verlag, Berlin, 334 pp.

Wilson, M.J. (1987) Soil smectites and related interstratified minerals: Recent developments. Pp. 167–173 in: *Proceedings of the International Clay Conference, Denver, 1985* (L.G. Schultz, H. van Olphen, and F.A. Mumpton, editors). The Clay Minerals Society, Bloomington, Indiana, USA.

Wray, J.J., Ehlmann, B.L., Squyres, S.W., Mustard, J.F., and Kirk, R.L. (2008) Compositional stratigraphy of clay-bearing layered deposits at Mawrth Vallis, Mars. *Geophysical Research Letters*, **35**, doi:10.1029/2008GL034385.

Yamada, H., Nakazawa, H., Yoshioka, K., and Fujita, T. (1991) Smectites in the montmorillonite-beidellite series. *Clay Minerals*, **26**, 359–369.

Yamada, H. and Nakazawa, H. (1993) Isothermal treatments of regularly interstratified montmorillonite-beidellite at hydrothermal conditions. *Clays and Clay Minerals*, **41**, 726–730.

Yang, K., Browne, P.L., Huntington, J.F., and Walshe, J.L. (2001) Characterising the hydrothermal alteration of the Broadlands-Ohaaki geothermal system, New Zealand, using short-wave infrared spectroscopy. *Journal of Volcanology and Geothermal Research*, **106**, 53–65.

(*Received 11 May 2010; revised 27 September 2011; Ms. 436; A.E. R. Milliken*)